

A $z \sim 1$ galactic-scale outflow transversally mapped to ~ 50 kpc through gravitational-arc tomography[★]

J. A. Hernández-Guajardo^{1**}, L. F. Barrientos¹, S. López², E. J. Johnston³, C. Ledoux⁴, N. Tejos⁵,
A. Afruni^{6,7}, M. Solimano³, E. Jullo⁸, H. Cortés-Muñoz², P. Noterdaeme⁹,
J. González-López¹, A. Ormazábal¹, F. Muñoz-Olivares¹, and T. A. M. Berg¹⁰

¹ Instituto de Astrofísica, Facultad de Física, Pontificia Universidad Católica de Chile, Av. Vicuña Mackenna 4860, 7820436 Macul, Santiago, Chile.

² Departamento de Astronomía, Universidad de Chile, Casilla 36-D, Santiago, Chile.

³ Instituto de Estudios Astrofísicos, Facultad de Ingeniería y Ciencias, Universidad Diego Portales, Av. Ejército Libertador 441, Santiago, Chile.

⁴ European Southern Observatory, Alonso de Córdova 3107, Vitacura, Casilla 19001, Santiago, Chile.

⁵ Instituto de Física, Pontificia Universidad Católica de Valparaíso, Casilla 4059, Valparaíso, Chile.

⁶ Dipartimento di Fisica e Astronomia, Università di Firenze, Via G. Sansone 1, 50019 Sesto Fiorentino, Firenze, Italy.

⁷ INAF - Osservatorio Astrofisico di Arcetri, Largo E. Fermi 5, Firenze, I-50125, Italy.

⁸ Aix-Marseille Univ., CNRS, CNES, LAM, Marseille, France.

⁹ Institut d'Astrophysique de Paris, CNRS-SU, UMR 7095, 98bis bd Arago, 75014 Paris, France.

¹⁰ Department of Physics and Astronomy, Camosun College, 3100 Foul Bay Rd, Victoria, B.C., V8P 5J2, Canada.

Received 5 September 2025 / Accepted 19 February 2026

ABSTRACT

We report spatially resolved measurements of cool gas traced by Mg II and Fe II absorption in the circumgalactic medium (CGM) of a star-forming galaxy at $z \sim 1$ (G1). The fortuitous alignment of a background gravitational arc at $z \sim 2.4$ provides seven closely spaced (~ 6 kpc) transverse sightlines along the minor axis of G1, probing its CGM out to ~ 50 kpc. This geometry allows us to detect a galactic-scale outflow simultaneously in down-the-barrel and transverse directions, where blue-shifted Mg II absorption is detected along both types of sightlines, revealing a large-scale, collimated wind. We measure blue-shifted line-of-sight velocities of $v_{\text{los}} \sim 62\text{--}239$ km s⁻¹ and line-of-sight velocity dispersions $\sigma_{\text{los}} \sim 53\text{--}133$ km s⁻¹, suggesting a structure dominated by bulk motion. De-projection of v_{los} along the minor axis indicates that the outflow material barely approaches the escape velocity and is likely to be gravitationally bound to G1. We constrain an outflow opening angle $\theta_o \sim 18^\circ\text{--}25^\circ$, and a mass outflow rate of $\dot{M}_{\text{out}} \gtrsim 0.06 M_\odot \text{ yr}^{-1}$, corresponding to a mass loading factor $\eta \gtrsim 0.004$, estimated within $\sim 10\text{--}50$ kpc ($\sim 0.05\text{--}0.3 R_{\text{vir}}$) of the galaxy centre. Our measurements, combined with previous arc tomography data along the major axis, indicate that normalizing impact parameters by galaxy B-band luminosity substantially reduces scatter in the established anti-correlation between Mg II equivalent width and impact parameter, while also diminishing possible excess of Mg II equivalent width towards the minor axis.

Key words. galaxies: evolution – galaxies: halos – galaxies: high-redshift – intergalactic medium – quasars: absorption lines

1. Introduction

The evolution of galaxies across cosmic time is driven by processes of inflows, outflows, and re-accretion of gas, collectively known as the baryon cycle. The circumgalactic medium (CGM) serves as the interface for these processes (see reviews by Tumlinson et al. 2017; Péroux & Howk 2020; Faucher-Giguère & Oh 2023). Outflows driven by supernovae, stellar winds, and active galactic nuclei (AGN) are key for regulating star formation, distributing metals and energy, and enriching the CGM with metals. Observationally, metal-enriched outflows are nearly ubiquitous in star-forming galaxies (e.g. Weiner et al. 2009; Rubin et al. 2010; Martin et al. 2012; Rubin et al. 2014), yet it remains unclear whether, and how efficiently, these outflows carry baryons to the CGM or beyond (e.g. Veilleux et al. 2020; Afruni et al.

2021). Answering these questions is crucial for understanding galaxy evolution, feedback, and the missing baryons problem.

One of the most widely used tracers of cool metal-enriched gas in the CGM is the Mg II $\lambda\lambda 2796, 2803$ doublet, and is arguably one of the best tracers of the cool ($T \sim 10^4$ K) metal-enriched CGM (Lanzetta et al. 1991; Steidel 1995; Churchill et al. 1996; Chen et al. 2010; Bordoloi et al. 2011; Nielsen et al. 2013b; Rubin et al. 2018; Lopez et al. 2018; Dutta et al. 2020; Lundgren et al. 2021). The Mg II doublet is efficiently observable from the ground over a wide redshift range, approximately $0.1 \lesssim z \lesssim 6$, even at moderate spectral resolution (e.g. Matejek & Simcoe 2012; Nielsen et al. 2013b; Huang et al. 2021). In emission, Mg II traces resonantly scattered photons, often revealing extended halos or outflows (e.g. Rubin et al. 2011; Burchett et al. 2021; Pessa et al. 2024). In absorption, strong ($W_0 > 0.3 \text{ \AA}$) systems are associated to ~ 100 kpc halos around star-forming galaxies (e.g. Chen et al. 2010; Bordoloi et al. 2011; Nielsen et al. 2013b), showing slow evolution with redshift (Lopez & Krogager 2025). Together, these properties establish the Mg II

[★] Based on observations collected at the European Southern Observatory under ESO programme 094.A-0141 (MUSE).

^{**} Corresponding author: joaquin.hernandezg@uc.cl

doublet as one of the most effective tracers for investigating the structure, kinematics, and evolution of the cool CGM throughout cosmic time.

Two complementary observational strategies have been historically used to probe gas flows in Mg II-bearing CGM, in absorption: down-the-barrel and quasar absorption lines. Down-the-barrel spectroscopy leverages the stellar continuum of the absorber galaxies themselves to probe gas along the line of sight toward the galaxy, and has revealed that outflows are ubiquitous and collimated (e.g. Rubin et al. 2014), having velocities of 100–1 000 km s⁻¹ (e.g. Tremonti et al. 2007; Weiner et al. 2009; Martin & Bouché 2009; Rubin et al. 2010; Coil et al. 2011; Martin et al. 2012; Bouché et al. 2012; Rubin et al. 2014; Heckman et al. 2015; Schroetter et al. 2016). Transverse absorption-line studies against background sources—usually quasars—probe gas at much larger galactocentric distances, typically tens to hundreds of kiloparsecs, at CGM scales (e.g. Nielsen et al. 2013b; Huang et al. 2021). These reveal that Mg II absorbers are more common and stronger around blue, star-forming galaxies than red, quiescent ones (Chen et al. 2010), and often align with either the major or minor axis of the host galaxy (e.g. Kacprzak et al. 2012; Martin et al. 2019; Lundgren et al. 2021), a bimodality that suggests a connection to inflows and outflows. However, both approaches have intrinsic limitations; down-the-barrel spectroscopy allows a straightforward discrimination between inflows and outflows, but provides no information about their spatial extent. Transverse absorption, on the other hand, constrains the spatial extent of the gas—through an impact parameter—but it is challenging to unambiguously associate the observed absorption kinematics with outflows, inflows, or other CGM processes.

In the era of 10m-class telescopes, deep integral field spectroscopy has opened the way for the use of extended background sources to resolve the CGM in absorption. Gravitational-arc tomography (Lopez et al. 2018) is a technique developed for studying the high-redshift CGM, leveraging bright gravitational arcs as extended background sources. This method effectively mimics many contiguous background sightlines, enabling spatially resolved spectroscopy of intervening gas associated with individual halos. Arc tomography results have shown—for the first time directly—that the CGM is clumpy and anisotropic (Lopez et al. 2018), and have revealed the presence of extended co-rotating disks (Lopez et al. 2020; Tejos et al. 2021) and signatures of outflows (Tejos et al. 2021; Mortensen et al. 2021; Fernandez-Figueroa et al. 2022; Shaban et al. 2025). Furthermore, the contiguous spatial information uniquely provided by arc tomography data has also provided constraints on the kpc-scale structure of the cool and warm CGM (Afruni et al. 2023; Lopez et al. 2024; Shaban et al. 2025). The rich spatial information provided by arc tomography offers a unique window to probe the structure and propagation of metal-enriched flows at CGM scales.

In this work, we present gravitational arc tomography along the projected minor axis of an intervening galaxy at $z \sim 1$, traced simultaneously by down-the-barrel and transverse absorption. This configuration arises from the fortuitous alignment between a bright background gravitational arc and a foreground star-forming galaxy at $z \sim 1$. It enables us to probe the possible outflowing gas both against the galaxy itself and, critically, along its minor axis—where outflows are expected to be most prominent and evident—over seven nearly contiguous sightlines spanning a ~ 50 kpc projected line.

Our paper is organized as follows. In Sect. 2, we describe observations. In Sect. 3, we describe the construction of the lens

model of the foreground galaxy cluster. In Sect. 4 we present the emission properties of the absorbing galaxy, based on *HST* imaging and MUSE spectroscopy. The absorption strength and kinematic measurements of the intervening gas are described in Sect. 5. Our main results are presented in Sect. 6 and discussed in Sect. 7. Throughout this paper, we assume a Λ CDM cosmology with the following parameters: $H_0 = 70$ km s⁻¹ Mpc⁻¹, $\Omega_m = 0.3$, and $\Omega_\Lambda = 0.7$. Magnitudes are reported in the AB system.

2. Observations

RCS 0224-0002 is a galaxy cluster at $z_{\text{cluster}} = 0.773$ discovered by the Red Cluster Sequence Survey (Gladders et al. 2002). The cluster acts as a gravitational lens for two background galaxies observed as extended and bright gravitational arcs at $z_A = 4.877$ and $z_B = 2.395$ (Gladders et al. 2002; Swinbank et al. 2007; Smit et al. 2017), hereafter referred to as “arc A” and “arc B”, respectively, and shown in Fig. 1. A star-forming galaxy at $z \approx 0.987$ (G1 from now on), is foreground and close in projection to arc B (see Fig. 1). Absorption features of Mg II and Fe II are detected at the redshift of G1 in the spectrum of arc B, which we interpret as cool CGM gas associated with G1, assuming the system is isolated.

2.1. HST imaging

We used archival Hubble Space Telescope (*HST*) imaging available in the Mikulski Archive for Space Telescopes (MAST), obtained under programs GO 14497 (PI: Smit) and GO 9135 (PI: Gladders). The system was observed with the Wide Field Planetary Camera 2 (WFPC2) in F606W (6×1.1 ks), the Advanced Camera for Surveys (ACS) in F814W (12×1.1 ks), and the Wide Field Camera 3 (WFC3) in F125W and F160W (each 2.6 ks). All images were reduced using Drizzlepac (Anand et al. 2025), re-sampling onto a common $0.03'' \text{ pix}^{-1}$ grid. A colour composite image using the F160W, F125W, and F814W filters is shown in Fig. 1.

2.2. MUSE spectroscopy

In this paper, we used archival integral-field spectroscopy from VLT/MUSE (Bacon et al. 2010) (Programme 094.A-0141, PI: Swinbank), observed between UT November 13, 2014, and September 16, 2016. We used the ESO MUSE pipeline (Weilbacher et al. 2012) in the ESO Recipe Execution Tool (EsoRex v2.8.3) environment (ESO CPL Development Team 2015) to reduce the data. As part of this routine, we created master bias, flat-field, and vacuum wavelength calibrations for each night using the associated raw calibrations provided by the Archive Facility. These master calibrations were applied to the raw science and standard-star observations as part of the pre-processing steps.

The reduced standard star observations were used to create a flux calibration solution for each night, which was applied to the science frames. The sky background was directly measured and subtracted from the individual science frames using spaxels identified as representing the sky. The flux-calibrated and sky-subtracted exposures were then combined to produce a single data-cube. The residual sky contamination was removed using the Zurich Atmosphere Purge code (ZAP, Soto et al. 2016). The final combined cube has a total exposure time of 3.75 hours with an average point spread function (PSF) full width at half maximum (FWHM) of $\approx 0.8''$ at 5500 Å, and a 1σ sensitivity of 1.6×10^{-20} erg s⁻¹ cm⁻² Å⁻¹ at ~ 5500 Å.

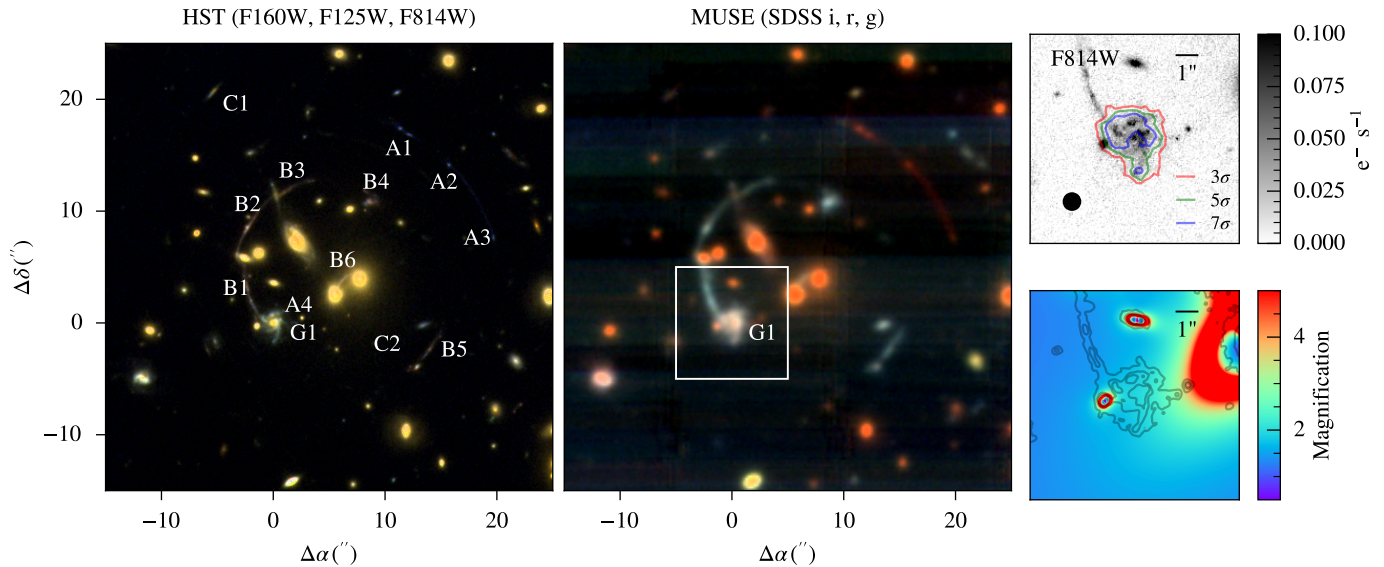


Fig. 1: *Left*: *HST* RGB (F160W, F125W, and F814W) image centred on the lensing cluster RCS 0224-0002. Labels indicate the position of G1, and the lensed sources reported by Smit et al. (2017), used for constraining the lens model. Redshifts of the lensed galaxies A, B, and C are 4.877, 2.395, and 5.498, respectively. *Centre*: MUSE RGB image constructed by convolving the cube with the transmission curves of the broad-band SDSS i , r , g filters. The white square, centred on G1, shows the size of the rightmost panels. *Top right*: *HST*/F814W cutout centred on G1. Red, green, and blue contours show the 3σ , 5σ , and 7σ levels where its [O II] emission is detected on the MUSE data. The typical PSF FWHM of $0.8''$ of the MUSE observations is represented by the diameter of the solid black circle. *Bottom right*: Magnification map centred on G1 showing the differential lensing effect at redshift of G1. Overlaid *HST*/F814W contours delineate the distribution of light from surrounding sources. Sources enclosing areas of higher magnification correspond to cluster member galaxies.

3. Strong lensing model

We constructed a strong lensing model of the foreground galaxy cluster to recover intrinsic spatial scales and physical properties in the absorber plane (i.e. at the redshift of G1). We guided the construction of our lens model by the one presented by Smit et al. (2017). The model was constrained using the positions and redshifts of multiple lensed sources identified in *HST* imaging and MUSE spectroscopy, including arcs A, B, and C, shown in Fig. 1. The redshift of arc A ($z_A = z_{[\text{O II}]} = 4.8760$), and arc B ($z_B = z_{\text{C III]} = 2.396$), were measured based on the nebular [O II] and C III] emission lines, respectively, by Smit et al. (2017), on their MUSE observations, where they also performed a blind survey of Ly α emitters, identifying the lensed source C, with $z_C = z_{\text{Ly}\alpha} = 5.498$.

The details of the strong lens modelling are presented in Appendix A. Our best-fit model achieves an image-plane RMS of $0.79''$, with a $\chi^2 = 13.7$ with 11 free parameters. We use this model to reconstruct the geometry in the absorber-plane and to correct the observed fluxes for lensing magnification. Due to its proximity along the line of sight to the lensing galaxy cluster, G1 is subject to small (but non-negligible) distortion and magnification from the strong lensing effect. In Fig. 1 we show the magnification map around G1, from which we measure an average magnification factor of $\mu = 1.89 \pm 0.07$ (areal average within the 3σ contour of the [O II] emission, shown in Fig. 1), a value that is robust to the specific lens model parametrization chosen for the analysis. For reconstructing the absorber-plane geometry, we applied the deflection matrices to the image-plane (i.e. as observed) positions, through the lens equation (see, e.g., Lopez et al. 2018). Impact parameters (ρ) are defined as the absorber-plane projected distances to the centre of G1. By sampling the deflection matrices from the posterior distributions of the model

parameters, we estimate a 1σ confidence interval of the deflections, which propagates into an uncertainty of 0.5 kpc on ρ in the absorber plane. Following Lopez et al. (2020), we arbitrarily adopt a total uncertainty of 1.5 kpc on the impact parameters, corresponding to half of the binned spaxel size in the absorber plane (see Sect. 5), in order to account for systematics (astrometry and lens model degeneracies).

4. G1 properties

This section details the photometric, kinematic, and stellar population properties of G1, which are summarized in Table 1.

4.1. Photometry and morphology

We performed aperture photometry on the *HST* imaging using SExtractor (Bertin & Arnouts 1996). The measured fluxes were corrected for lensing magnification, dividing the integrated fluxes by the average magnification, and for Galactic extinction, using the recalibration from Schlafly & Finkbeiner (2011) to the dust extinction maps from Schlegel et al. (1998), assuming an F99 (Fitzpatrick 1999) dust extinction law. The rest-frame B-band luminosity was estimated from the *HST* F814W band, corresponding to the B-band at $z \sim 1$. We assumed a characteristic rest-frame B-band absolute magnitude $M_B^* = -21.416$ at $z \sim 1$ by interpolating the B-band luminosity function from Willmer et al. (2006). We find that G1 has a luminosity of $L_B = 2.6 L_B^*$, above the characteristic luminosity at $z \sim 1$.

We used GALFIT (Peng et al. 2002) on the de-lensed F814W data to analyse the rest-frame B-band flux profile of G1, fitting a single Sérsic component with all parameters free. The best-fit Sérsic index is $n \approx 1.2 \pm 0.2$, consistent with an exponential

disk profile. We estimated the inclination angle from the axis ratio q , assuming an infinitely thin disk ($\cos i = q$). The Sérsic index, axis ratio, position angle (PA), and effective radius (R_e) are listed in Table 1, while the best-fit model and residuals are shown in Fig. 2. The residuals reveal spiral features and compact star-forming clumps, indicative of a clumpy, gas-rich disk. Such structures are typical of high-redshift disks undergoing active star formation (Elmegreen et al. 2005; Law et al. 2007; Förster Schreiber et al. 2009; Guo et al. 2015; Shibuya et al. 2016; Kalita et al. 2025).

4.2. Stellar and halo properties

We used BAGPIPES (Carnall et al. 2018, 2019) to model the spectral energy distribution (SED) of G1, jointly fitting its MUSE and *HST* photometry. The resulting stellar mass and SFR, and their respective errors were inferred from the posterior distributions. Additionally, the star formation rate (SFR) was independently estimated via the [O II] luminosity, using the calibration from Kennicutt (1998). Both SFR estimates agree within 1σ and are listed in Table 1. With a specific SFR of $7.58 \times 10^{-10} \text{ yr}^{-1}$, G1 lies on top of the star-forming main sequence at $z \sim 1$ (Popesso et al. 2023).

Next, from the inferred stellar mass, we estimate a total halo mass M_h using the stellar-mass-halo-mass (SMHM) relation from Moster et al. (2010). Finally, we estimated the respective virial radius R_{vir} , maximum circular velocity V_{circ} , escape velocities $V_{\text{esc}}(r)$, and dark matter (DM) halo velocity dispersion σ_{DM} . All these properties are listed in Table 1, and the details of the methodology are described in more detail in Appendix B.

4.3. Morpho-kinematic modelling

As shown in Fig. 1 (top right), the [O II] emission of G1 is spatially resolved in the MUSE data, given the average $\sim 0.8''$ PSF FWHM of the MUSE data, and the optical diameter of G1 being $\sim 2''$. We do not detect extended [O II] emission beyond the stellar disk, which is expected given the exponential decrease in the surface brightness profile of ionized gas emission (e.g. Nielsen et al. 2024). Given the spectral resolution of MUSE (FWHM of $\sim 50 \text{ km s}^{-1}$ at the rest-frame of [O II] at $z \sim 1$), we are able to resolve the [O II] doublet and recover spatially resolved kinematics, as observed in the centroid-velocity-map of the [O II] emission shown in Fig. 3 (black rhomboids). The [O II] velocity field clearly resembles a typical rotating disk (e.g. Guérou et al. 2017; Patrício et al. 2018).

We modelled the disk kinematics of G1 in the absorber plane using GalPak^{3D} (Bouché et al. 2015). We first de-lensed the MUSE data by applying the deflections from the lens model, reconstructing the absorber-plane emission on a regular grid with the native MUSE spaxel size of $0.2''$, following the method described in Tejos et al. (2021). The kinematics was modelled assuming an arctan rotation curve and the surface brightness with an exponential profile. The best-fit model parameters; systemic redshift ($z_{[\text{O II}]}$), maximum rotation velocity (v_{max}), turnover radius (r_{to}), effective radius (R_e), intrinsic gas velocity dispersion (σ_{gas}), inclination (i), and position angle (PA), are listed in Table 1. Hereafter, we adopt $z_{[\text{O II}]}$ as the systemic redshift of G1 ($z_{\text{G1}} = z_{[\text{O II}]}$).

The best-fit PA and R_e of the [O II] emission agree with those obtained from GALFIT within 2σ . We use the GalPak^{3D} PA to define the kinematic major and minor axes of G1, shown in Figs. 3 and 4. However, the i derived from GalPak^{3D} (65.5°)

differs by $\sim 50\%$ from that inferred via the axis ratio (42.3°). Since the kinematic model incorporates both morphological and kinematic constraints, it provides a more reliable estimate of the inclination; thus, we adopt the GalPak^{3D}-derived i as the fiducial value.

The r_{to} value is unusually small, likely because the [O II] emission is weaker in the central regions of G1 and dominated by the clumps (Fig. 1), limiting the model's sensitivity to the inner velocity gradient. As a result, the modelling of the inner velocity structure may be more uncertain; however, the large-scale kinematic parameters— v_{max} , PA, and i —remain robust, as they are primarily constrained by the outer regions with stronger [O II] emission. In the case of σ_{gas} the small value of $\sim 10 \text{ km s}^{-1}$ is consistent with expectations for cool ionized gas in star-forming disks.

Altogether, the morphological, kinematic, and stellar population properties of G1 point to a typical main-sequence disk galaxy at $z \sim 1$, unperturbed by major interactions, undergoing sustained star formation. Indeed, we do not find any companion galaxy within 3000 km s^{-1} of z_{G1} in the MUSE field of view ($\sim 500 \text{ kpc} \times 500 \text{ kpc}$ at z_{G1}), and thus, we assume that G1 is an isolated galaxy. These properties provide essential context for interpreting the intervening metal absorption lines.

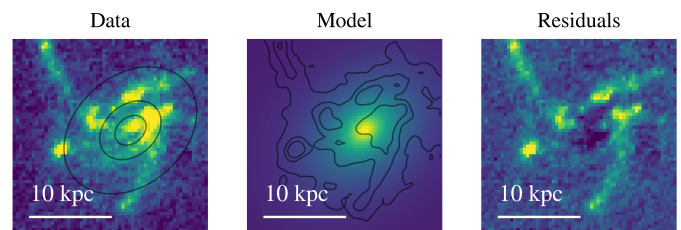


Fig. 2: *Left*: De-lensed F814W cutout centred on G1. Black contours show representative flux levels of the best-fit Sérsic model. *Centre*: Best-fit single-component Sérsic model obtained with GALFIT. Black contours indicate the same flux levels as in the left panel. Best-fit R_e , PA, q , and n values are listed in Table 1. *Right*: Flux residuals from the best-fit model.

5. Intervening absorption properties

Intervening Mg II $\lambda\lambda 2796, 2803$ and Fe II $\lambda\lambda 2586, 2600$ absorptions at $z_{\text{abs}} \sim z_{\text{G1}}$ are detected over the B1 and B2 images of arc B, and over G1. To measure the absorption-lines properties, we apply 4×4 spatial binning to the native $0.2''$ MUSE spaxels, following Lopez et al. (2018). This yields binned spaxels of $0.8''$, spaced by at least one PSF FWHM, balancing the need to boost S/N and minimize spaxel cross-talk, while preserving sufficient spatial resolution to map the intervening absorptions. We define a mask enclosing G1, and the B1–B6 arc images, and retain only those binned spaxels with continuum S/N ≥ 2 near the Mg II spectral region for the subsequent analysis.

We fit the combined Mg II and Fe II absorption spectrum using four Gaussian components, one per transition. The velocity centroid and dispersion were tied for all four lines, under the assumption that they trace gas with similar properties (e.g., Churchill & Vogt 2001). For each ion, the relative amplitudes of the two transitions were allowed to vary between the optically thin limit (set by the ratio of their oscillator strengths) and the optically thick limit (unity ratio). With $R \sim 2000$ at 5500 \AA , MUSE lacks the resolution to de-blend individual narrow kinematic

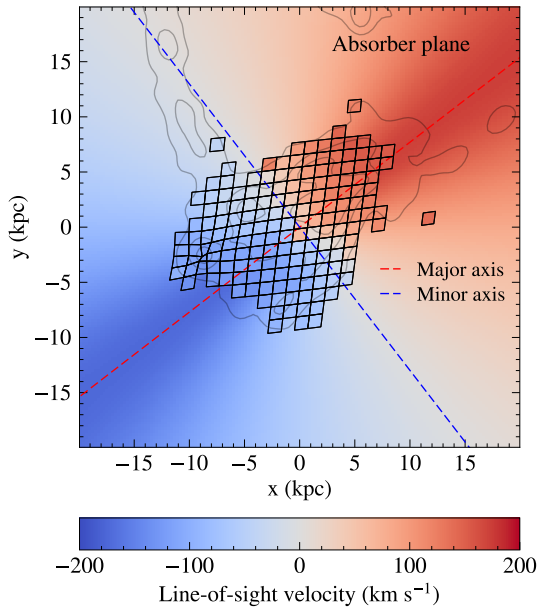


Fig. 3: De-lensed (absorber-plane) centroid-velocity-map of the [O II] emission from G1 and ERD model kinematics. Zero velocity is set at z_{G1} . Open rhomboids indicate native MUSE spaxels mapped into the absorber plane, with colours representing the measured line-of-sight [O II] velocity centroid. The background colourmap shows the line-of-sight velocity field from the best-fit arctan disk model obtained with GalPak^{3D}. Dashed lines mark the kinematics major (red) and minor (blue) axes of G1. Grey contours trace the *HST*/F814W flux distribution. Note that the spaxel-based velocities are shown for illustrative purposes only: GalPak^{3D} does not extract velocities per spaxel, but fits a synthetic data-cube—convolved with the instrumental line spread function and PSF—which is directly compared to the observed cube.

components; hence, each transition is modelled with a single Gaussian component. The line-of-sight velocity (v_{los}) and velocity dispersion (σ_{los}) are then derived from the Gaussian centroid and width, respectively, with the latter corrected for instrumental broadening by subtracting the line spread function in quadrature. Rest-frame equivalent widths ($W_r = \sqrt{2\pi}A\sigma/(1+z_{\text{abs}})$) were calculated in the continuum-normalized spectrum from the Gaussian parameters σ and A (standard deviation and amplitude, respectively) at the rest-frame of G1. The continuum level was independently measured for each transition on 100 Å windows on both the blue and red sides of the absorption features. The 1σ uncertainties in W_r (σ_{W_r}) were derived through the propagation of the uncertainties in A and σ .

We define a significant detection as having a rest-frame equivalent width significance $W_r/\sigma_{W_r} \geq 2$ in at least two transitions. For spaxels meeting the S/N but lacking significant detections, we report 2σ upper limits: $2\sigma_{W_r}$, where $\sigma_{W_r}(1+z_{\text{abs}}) = \text{FWHM}/\langle S/N \rangle$, following Lopez et al. (2018). We detect significant absorption on seven transverse and 13 down-the-barrel sightlines. While the rather loose S/N pre-selection ($S/N \geq 2$) ensured scanning of all arc spaxels, the final classification of detections is automated and based on the above significance criterion. In Figs. F.1 and G.1 we show the image-plane binned spaxels and their fitted Gaussian profiles (when $S/N \geq 2$), for Mg II and Fe II, respectively. Only spaxels in arcs B1, B2, and over G1 show significant absorptions. The derived v_{los} val-

Table 1: G1 properties

Magnification	$\mu = 1.89 \pm 0.07$
<i>From [O II] emission and broad-band imaging (see Sect. 4)</i>	
Right Ascension	RA = 02h24m34.10s
Declination	DEC = -00d02m30.9s
Effective radius (Stars) ^{a,e}	$R_e = 8.1 \pm 1.2$ kpc
Position angle (Stars) ^{a,e}	PA = $130.7 \pm 2.3^\circ$
Axis ratio (Stars) ^{a,e}	$q = 0.739 \pm 0.015$
Inclination (Stars) ^{a,e,f}	$i = 42.3 \pm 1.3^\circ$
Sérsic index (Stars) ^{a,e}	$n = 1.2 \pm 0.2$
Apparent magnitude (F814W) ^{b,e}	$m_B = 20.97 \pm 0.16$
Absolute magnitude (~B band) ^{b,e}	$M_B = -22.47 \pm 0.16$
Luminosity (~B band) ^{b,e}	$L_B = 2.6 \pm 0.4 L_B^*$
Stellar mass ^b	$\log(M_*/M_\odot) = 10.29 \pm 0.01$
SFR from SED ^b	$\text{SFR}_{\text{SED}} = 15.05 \pm 0.27 M_\odot \text{ yr}^{-1}$
SFR from [O II] ^{b,c}	$\text{SFR}_{[\text{O II}]} = 15 \pm 4 M_\odot \text{ yr}^{-1}$
Specific SFR ^b	$\text{sSFR}_{\text{SED}} = (7.58 \pm 0.29) \times 10^{-10} \text{ yr}^{-1}$
[O II] Luminosity ^b	$L_{[\text{O II}]} = (9.45 \pm 0.05) \times 10^{41} \text{ erg s}^{-1}$
<i>From morpho-kinematical analysis of [O II] emission (see Sect. 4.3)</i>	
Systemic redshift	$z_{G1} = z_{[\text{O II}]} = 0.986790 \pm (4 \times 10^{-6})$
Maximum rotation velocity (Gas)	$v_{\text{max}} = 191 \pm 2 \text{ km s}^{-1}$
Turnover radius (gas) ^a	$r_{\text{to}} = 1.96 \pm 0.08 \text{ kpc}$
Position angle (gas) ^a	PA = $127.6 \pm 0.3^\circ$
Inclination (gas) ^a	$i = 65.5 \pm 0.3^\circ$
Velocity dispersion (gas) ^a	$\sigma_{\text{gas}} = 12.4 \pm 1.2 \text{ km s}^{-1}$
Effective radius (gas) ^a	$R_e = 8.38 \pm 0.05 \text{ kpc}$
<i>Halo properties</i>	
Halo mass	$\log(M_h/M_\odot) = 12.1 \pm 0.1$
Virial radius	$R_{\text{vir}} = 159 \pm 13 \text{ kpc}$
Dark matter halo velocity dispersion	$\sigma_{\text{DM}} \approx 104 \text{ km s}^{-1}$
Halo maximum circular velocity ^g	$V_{\text{circ}} \approx 200 \text{ km s}^{-1}$
Escape velocity ^g	$V_{\text{esc}}(r = 10 \text{ kpc}) \approx 560 \text{ km s}^{-1}$
Escape velocity ^g	$V_{\text{esc}}(r = 50 \text{ kpc}) \approx 460 \text{ km s}^{-1}$

Notes.

- (a) In the reconstructed absorber plane.
- (b) De-magnified quantity using $\mu = 1.89$.
- (c) Obscured.
- (d) Defined from the arctan rotation curve: $v(r) = v_{\text{max}} \arctan(r/r_{\text{to}})$.
- (e) From *HST*/F814W imaging.
- (f) Assuming negligible disk intrinsic thickness.
- (g) Assuming a NFW profile with concentration parameter 5.

ues are measured with respect to z_{G1} , and span a range of $\approx [-60, -240] \text{ km s}^{-1}$ across all sightlines.

Absorber-plane impact parameters ρ and azimuthal angles ϕ are defined relative to G1's de-lensed centroid and receding major axis, respectively, following Tejos et al. (2021). Table E.1 details the absorption properties measured on each spaxel and Fig. 4 shows the spatial distribution of the spaxels with detected absorptions, in the image plane, and $W_r(2796)$, v_{los} , and σ_{los} , in the absorber plane, for the Mg II absorptions. These spatially resolved absorption maps serve as the basis for our results presented in the following section.

6. Results

The absorptions detected over arc B, and G1, exhibit similar velocities. Given that G1 is an isolated galaxy, we hereafter assume G1 is responsible for the intervening Mg II and Fe II absorption detected in the background arc B (see Sect. 5). Thus, spaxels

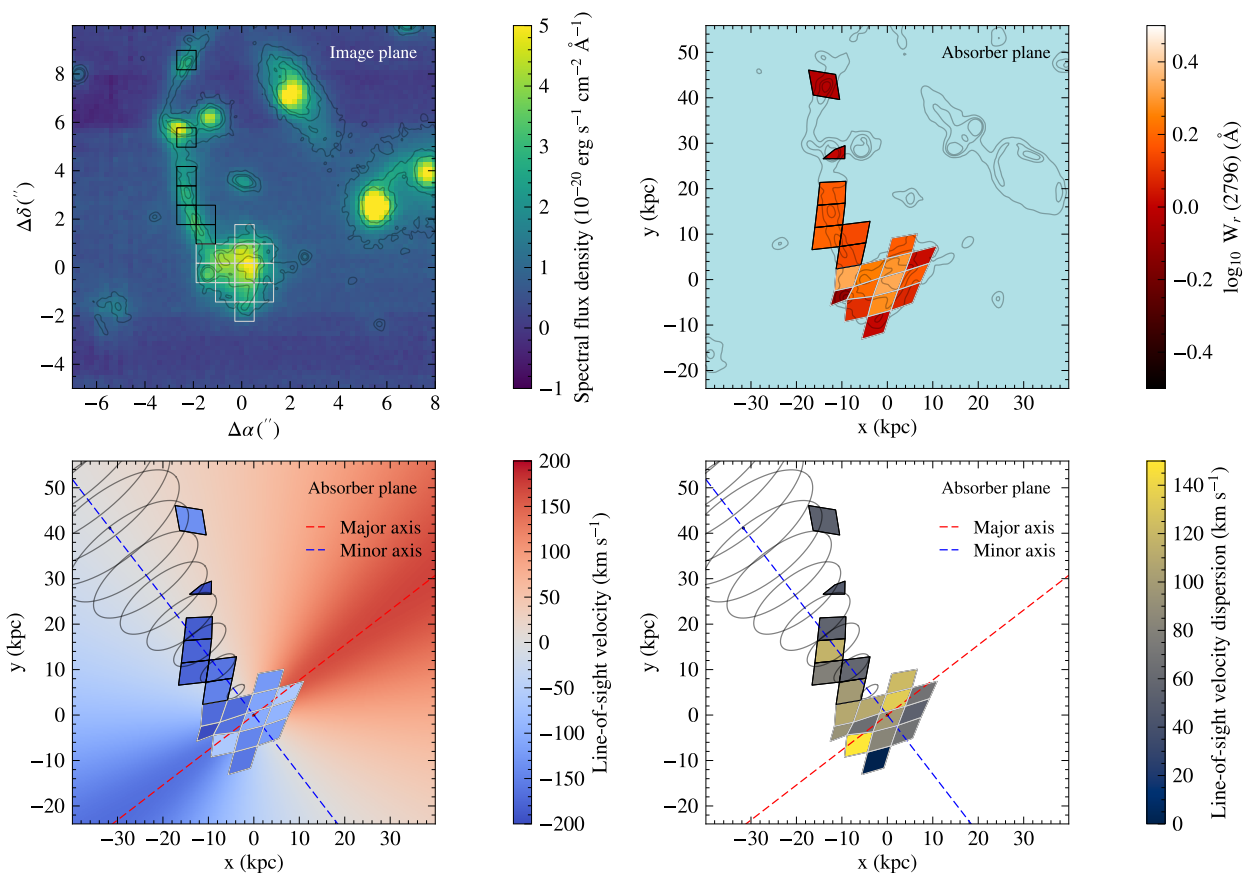


Fig. 4: *Top left*: Image-plane (i.e., as observed) MUSE pseudo-broad-band image (SDSS r) around G1 and the background gravitational arc B. Open squares show the 4×4 binned spaxels with detected Mg II absorption. Spaxels with black (white) edges correspond to transverse (down-the-barrel) sightlines. *Top right*: Absorber-plane (de-lensed) distribution of the measured Mg II equivalent widths $W_r(2796)$. Contours of the de-lensed *HST*/F814W image of the field are shown for spatial reference. Cluster galaxies and other non-lensed sources should not appear in the absorber plane, but we included them in the contours to provide a spatial reference. *Bottom left*: Absorber-plane distribution of the Mg II line-of-sight velocities with respect to z_{G1} . The background colourmap shows the projected line-of-sight velocity of a rotating extended disk model for G1. The kinematic major and minor axes of G1 are indicated with the red and blue dashed lines, respectively. Black solid ellipses show a schematic model of a conical outflow along the minor axis of G1, with opening angle $\theta_c = 17.8^\circ$ and inclination $i = 65.5^\circ$. *Bottom right*: Absorber-plane distribution of the Mg II line-of-sight velocity dispersion after subtracting the MUSE instrumental line spread function. Black curves and red and blue dashed lines indicate the same outflow model and kinematics axes of G1 as in the bottom left panel.

probing the continuum of arc B provide transverse sightlines, probing the CGM of G1, whereas those intersecting G1’s own stellar continuum provide down-the-barrel measurements of the intervening gas directly in front of G1. The transverse sightlines span impact parameters in the range ~ 10 – 50 kpc, corresponding to ~ 0.05 – $0.3 R_{\text{vir}}$, and are closely aligned with the minor axis of G1 ($\phi \sim 90^\circ$).

6.1. Absorption strength

Figure 5 (panel a) shows $W_r(2796)$ as a function of ρ . We compare our transverse $W_r(2796)$ measurements to both quasar-galaxy pairs (Nielsen et al. 2013b; Huang et al. 2021) and other arc tomography systems (Lopez et al. 2018, 2020; Tejos et al. 2021; Shaban et al. 2025). Our measurements fall within the scatter of the quasar statistics (Huang et al. 2021) and the log-linear fit from Nielsen et al. (2013b), and are also encompassed by the scatter of the ensemble of arc tomography systems (Lopez et al. 2018, 2020; Tejos et al. 2021; Shaban et al. 2025). We exclude the down-the-barrel measurement from the $W_r(2796)$ – ρ

analysis because impact parameters are not defined for this geometry and these sightlines cross half of the CGM from the inside out.

A Pearson correlation analysis for $W_r(2796)$ vs. ρ yields a Pearson correlation coefficient $r_p = -0.75$, and p-value $p = 0.026$, confirming a statistically significant anti-correlation, a trend that aligns with previous quasar and arc-based measurements (e.g. Nielsen et al. 2013a; Huang et al. 2021; Lopez et al. 2018). In terms of normalization, our $W_r(2796)$, measured along the minor axis, lie near the upper envelope of the $W_r(2796)$ – ρ space of the combined arc tomography systems over the ~ 10 – 50 kpc range.

6.2. Absorption kinematics

Both down-the-barrel and transverse absorptions along G1’s minor axis exhibit comparable velocities with down-the-barrel line-of-sight velocities spanning $v_{\text{los,dtb}} = [-63, -239]$ km s $^{-1}$ and transverse velocities spanning $v_{\text{los,\perp}} = [-134, -197]$ km s $^{-1}$ (Fig. 4 and Table E.1). The blue-shifted down-the-barrel ab-

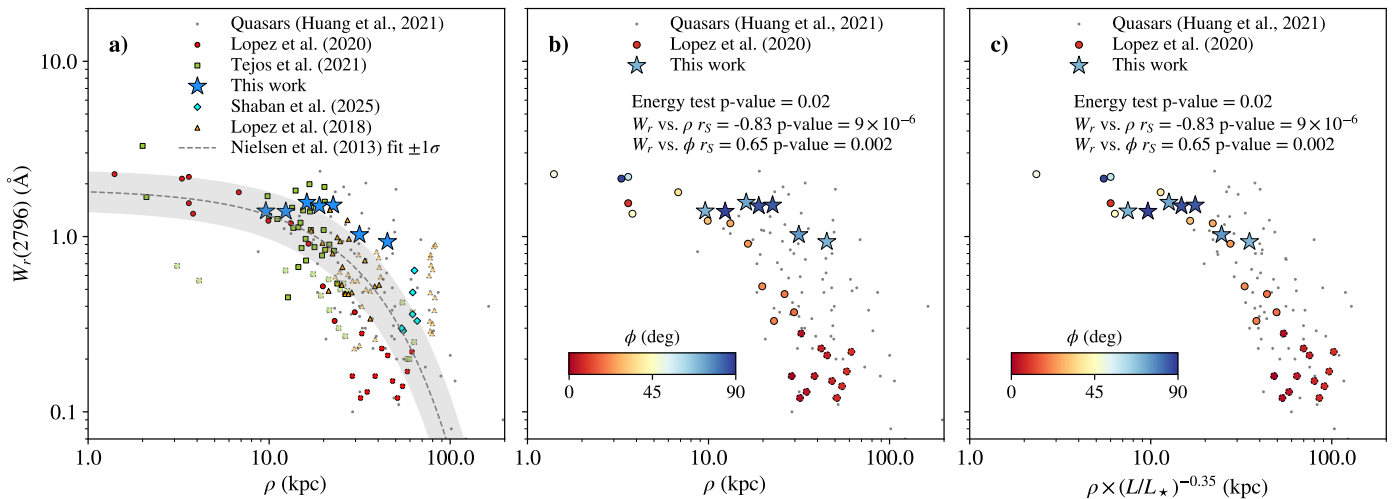


Fig. 5: *Panel a*: Rest-frame Mg II equivalent width, $W_r(2796)$, as a function of impact parameter, ρ , to the absorber galaxy. Our arc tomography measurements are shown as blue stars. Black dots represent quasar-galaxy pairs at $z \lesssim 0.5$ from Huang et al. (2021). The gray dashed line and shaded region correspond to the log-linear fit ($\pm 1\sigma$) from Nielsen et al. (2013b) based on the MAGIICAT sample at $0.07 \leq z \leq 1.1$. Coloured and semi-transparent symbols show individual measurements and upper limits, respectively, from gravitational arc systems from Lopez et al. (2018), Lopez et al. (2020), Tejos et al. (2021), and Shaban et al. (2025). *Panel b*: Comparison between the system presented in this work (probed primarily along the minor axis) and the system from Lopez et al. (2020) (probed along the major axis). Symbols are coloured by azimuthal angle, ϕ , of each sightline relative to the galaxy’s major axis. Overlaid are the results of statistical analyses, including the Energy test statistic and partial Pearson correlation coefficients between $W_r(2796)$ and ρ , and $W_r(2796)$ and ϕ . *Panel c*: Same as Panel b, but with impact parameters scaled by galaxy B-band absolute magnitude using Eq. 2, following Chen et al. (2010)

sorptions alone already indicate the presence of outflowing gas (e.g. Rubin et al. 2014), and the coherent blueshifts along G1’s minor axis sightlines indicate this outflow extends to tens of kpc (i.e. CGM scales; alternative scenarios are discussed in Sect. 7.1.2). The velocity range probed by $v_{\text{los,dtb}}$ is comparable to that spanned $v_{\text{los,L}}$, although $v_{\text{los,dtb}}$ extends to slightly lower velocities. This likely reflects contributions from absorbing components at or near the systemic velocity of G1, which are unresolved in our data.

Interpreting the CGM kinematics requires placing the absorption velocities in the context of the host galaxy dynamics. Previous studies have shown that strong Mg II absorbers may either co-rotate with the stellar disk of the host galaxy (e.g. Ho et al. 2017; Zabl et al. 2019) or trace collimated outflows at kiloparsec scales (e.g. Kacprzak et al. 2014; Zabl et al. 2020). In most galaxy–quasar pair studies, however, these scenarios remain difficult to distinguish because each galaxy is usually probed by a single transverse sightline. Gravitational-arc tomography overcomes this limitation by providing multiple contiguous sightlines through the CGM. Indeed, previous arc tomography studies have revealed cases of CGM gas co-rotating with the stellar disk (Lopez et al. 2020; Tejos et al. 2021; Fernandez-Figueroa et al. 2022).

To test the co-rotation scenario, we constructed an extended rotating disk (ERD) model following Tejos et al. (2021), based on the kinematic model of G1. Starting from the parameters of the arctan model (PA, r_f , v_{max} , i), we extrapolated the projected velocity field beyond the stellar disk. The resulting ERD line-of-sight velocity field is shown along with the [O II] centroid-velocity-map in Fig. 3, and with the absorption kinematics in Fig. 4 (panel c). The absorption velocities clearly differ from those predicted by the ERD model, indicating that the gas kinematics is not explained by disk co-rotation. Although the ERD model does not account for beam-smearing effects introduced by

the PSF, this limitation does not affect the qualitative conclusion, as the velocity offsets between the data and the model are large and systematic.

Finally, the absorption kinematics exhibit a remarkable degree of coherence. v_{los} and σ_{los} show little scatter across the transverse sightlines, with the scatter in v_{los} of $\sigma_{v,\text{los}} \approx 20 \text{ km s}^{-1}$, and the scatter in σ_{los} of $\sigma_{\sigma,\text{los}} \approx 24 \text{ km s}^{-1}$. Notably, the $\sigma_{v,\text{los}}$ value, is a factor of ~ 4 smaller than the mean velocity dispersion $\bar{\sigma}_{\text{los}} \approx 72 \text{ km s}^{-1}$. Together, these properties point to a coherent, large-scale, blue-shifted structure extending across tens of kpc, consistent with the presence of a galactic-scale outflow pointing toward the observer.

6.3. Outflow interpretation

6.3.1. Outflow geometry

The predominantly blue-shifted Mg II absorptions relative to G1’s systemic velocity argue strongly against an isotropic outflow. In such a scenario, we would expect symmetric absorption profiles in the transverse direction—combining contributions from both the approaching and receding sides of the outflow bubble—and velocity centroids close to the systemic redshift. However, none of the transverse sightlines show significant absorption at redshifted velocities (Fig. F.1). This, together with the blue-shifted down-the-barrel absorptions, indicates that the absorbing material lies entirely on the near side of the galaxy and that the outflow is collimated rather than spherical.

To understand the spatial configuration of the outflowing gas, we model the outflow as a bi-conical structure originating from the galaxy centre (e.g., Gauthier & Chen 2012). We use the azimuthal angles of the transverse sightlines (Table E.1) to constrain the outflow opening angle. To intercept all transverse absorptions, the cone must have a minimum half-opening angle of

$\theta_{c,\min} = 17.8^\circ$. Assuming uniform gas density within the cone (following Chen et al. 2014) and accounting for galaxy inclination, the geometry must satisfy $i + \theta_c \lesssim 90^\circ$ to avoid redshifted transverse absorptions, which restricts the maximum opening angle to $\theta_{c,\max} \sim 24.5^\circ$. A schematic of the inferred geometry is shown in Fig. 4.

This narrow opening angle ($\sim 18^\circ$ – 25°) lies below typical statistical averages of $\sim 50^\circ$ from outflow detection rates in inclined galaxies (Martin et al. 2012; Rubin et al. 2014), but aligns with individual quasar-based constraints of $\sim 6^\circ$ – 56° (Gauthier & Chen 2012; Schroetter et al. 2019) and arc tomography estimates ($\theta \sim 36^\circ$; Fernandez-Figueroa et al. 2022). Extended background sources sampling a wider range of azimuthal angles (e.g., Tejos et al. 2021; Fernandez-Figueroa et al. 2022) will be essential to constrain outflow geometries more tightly.

6.3.2. Outflow velocity profile

The unique alignment of the background arc with G1’s minor axis allows us to trace outflow velocities all the way from the disk of G1 to CGM scales. Assuming a collimated wind (Rubin et al. 2014; Martin 2005; Weiner 2009; Martin et al. 2012) outflowing perpendicular to the disk of G1, transverse impact parameters were de-projected into a radial distance, $r = \rho / \sin i \approx 1.1 \times \rho$, to the centre of G1. Line-of-sight velocities were likewise de-projected as $v_{\text{depr}} = v_{\text{los}} / \cos i \approx 2.4 \times v_{\text{los}}$.

With these assumptions, we obtain de-projected velocities of $v_{\text{depr,dtb}} = 150$ – 576 km s^{-1} for the down-the-barrel sightlines, and $v_{\text{depr,\perp}} = 318$ – 477 km s^{-1} for the transverse ones. In Fig. 6, we show $v_{\text{los,\perp}}$, $v_{\text{los,dtb}}$, σ_{los} , $v_{\text{depr,\perp}}$, and $v_{\text{depr,dtb}}$ as a function of r . For the down-the-barrel sightlines, we arbitrarily set $r = 0$ because the physical scales probed by these sightlines are unknown, while explicitly not assuming that the absorption originates at this distance.

Using the dark-matter halo model described in Sect. 4.2 and Appendix B, we computed the expected escape-velocity profile $V_{\text{esc}}(r)$, also shown in Fig. 6. The $v_{\text{depr,\perp}}$ values approach but do not exceed $V_{\text{esc}}(r)$, suggesting that the outflowing material is consistent with being gravitationally bound to G1. Similarly, the $v_{\text{depr,dtb}}$ lie below $V_{\text{esc}}(r)$ for $r < 0.3 R_{\text{vir}}$, with the exception of a single sightline that may exceed the escape velocity depending on the (unknown) radius at which the absorption is produced.

The $v_{\text{depr,\perp}}$ (and $v_{\text{los,\perp}}$) values increase with radius up to $\sim 0.2 R_{\text{vir}}$ before declining near $\approx 0.3 R_{\text{vir}}$, suggesting an initially accelerating and then decelerating wind structure. The apparent decline in velocity observed in Fig. 6, although supported by only one point, is consistent with previous observations. For example, Kacprzak et al. (2014) report blue-shifted down-the-barrel velocities of 45 – 255 km s^{-1} in a $z \sim 0.2$ galaxy with comparable stellar mass and SFR, but significantly lower transverse velocities (40 – 80 km s^{-1}) at $\rho \sim 58 \text{ kpc}$, suggesting outflow deceleration at large radii.

To interpret the velocity profile, we adopt a simple momentum-driven wind model (Murray et al. 2005), which has been shown to provide a reasonable description of the kinematics of cool outflows traced by low-ionization absorption lines (e.g. Heckman et al. 2015). Following Heckman et al. (2015), the inward force is given by the gravitational potential $\phi(r)$ and the cloud mass M_c as $F_{\text{in}} = -M_c \nabla \phi(r)$, while the outward force is $F_{\text{out}} = A_c \dot{p}_\star / 4\pi r^2$. Here, $\dot{p}_\star = 4.8 \times 10^{33} \times (\text{SFR} / M_\odot \text{yr}^{-1})$ dyne, is the momentum injection rate from star formation, $M_c = A_c N_H \mu m_p$ is the mass of an outflowing cloud, with A_c its cross section, N_H its hydrogen column density, μ the mean particle

mass in units of the proton mass m_p (we adopt $\mu \approx 1.6$, Veilleux et al. 2020). The net force is thus given by $F = F_{\text{out}} - F_{\text{in}} = v(r) [dv(r)/dt]$. Solving for the radial velocity profile

$$v(r) = \sqrt{v_0^2 + 2[\phi(r_0) - \phi(r)] + 2 \frac{\dot{p}_\star}{4\pi\mu m_p N_H} \left[\frac{1}{r_0} - \frac{1}{r} \right]} \quad (1)$$

where the only free parameters are a normalization v_0 at a given r_0 , and N_H , for a given gravitational potential model. Again, we assume the same dark-matter halo model used for estimating $V_{\text{esc}}(r)$. The parameters r_0 and v_0 should not be interpreted as the physical launch radius or initial velocity of the outflow, but rather as normalization parameters of the adopted equation of motion.

A least-squares fit to $v_{\text{depr,\perp}}$ vs. r results in $r_0 = 5.25 \text{ kpc}$, $v_0 = 116 \text{ km s}^{-1}$, and $\log(N_H/\text{cm}^{-2}) = 19.96$. The best-fit momentum-driven model trajectory is shown in Fig. 6, and is consistent at a $< 1.5\sigma$ level with all the transverse data points, capturing the initial acceleration, the subsequent decline in velocity, and the sub-escape velocities. We discuss the implications of the outflow radial velocity profile in Sect. 7.1.1.

6.3.3. Mass outflow rate

With the geometry and kinematics of the outflow characterized, we estimated the associated mass outflow rate. Assuming a thin-shell bi-conical geometry, the instantaneous mass outflow rate at radius r is $\dot{M}_{\text{out}} = \Omega \mu m_p N_H v r$, where $\Omega = \Omega_{\text{outflow}} C_f$ is the effective solid angle subtended by the outflow, modified by the cloud covering fraction C_f . As seen from the galaxy, $\Omega_{\text{outflow}} = 4\pi(1 - \cos \theta)$ for a bi-conical structure. Here, $\mu \approx 1.6$ is the mean mass per hydrogen atom (accounting for the helium fraction; Veilleux et al. 2020), m_p is the proton mass, N_H is the total hydrogen column density, and v is the outflow velocity at radius r (Rupke et al. 2005; Veilleux et al. 2020).

We adopted a conservative lower limit on $N_{H,1}$ derived in Sect. C using Eq. C.1 and Eq. C.2, and assume $N_H = N_{H,1}$. With our constraint on the minimum opening angle, we obtained $\Omega_{\text{outflow},\min} \approx 0.6 \text{ sr}$. Also, we assumed $C_f \approx 0.7$ (Berg et al. 2025) measured for Mg II absorptions against gravitational arcs. Considering the r and $v_{\text{depr,\perp}}$ values from Sect. 6.3.1, we estimate a minimum mass outflow rate $\dot{M}_{\text{out},\min}(r)$, which ranges from $\approx 0.06 M_\odot \text{yr}^{-1}$ at $\rho \approx 10 \text{ kpc}$, to $\approx 0.21 M_\odot \text{yr}^{-1}$ at $\rho \approx 45 \text{ kpc}$.

From our lower limits on $\dot{M}_{\text{out},\min}$ we estimate minimum mass loading factors of $\eta_{\min} = \dot{M}_{\text{out},\min} / \text{SFR} \approx (0.4\text{--}1.5) \times 10^{-2}$. Similarly, for the maximum opening angle, the minimum mass outflow rate increases to $\dot{M}_{\text{out},\min} \approx (0.12\text{--}0.4) M_\odot \text{yr}^{-1}$ and $\eta_{\min} \approx (0.8\text{--}2.7) \times 10^{-2}$. These lower limits are broadly consistent with quasar-traced galactic outflows from MEGAFLOW (Schroetter et al. 2019) and similar studies (e.g., Bouché et al. 2012; Heckman et al. 2015; Martin et al. 2019). Such works typically report $\dot{M}_{\text{out}} \sim 0.1\text{--}10 M_\odot \text{yr}^{-1}$ and $\eta \sim 0.1\text{--}10$, albeit with significant scatter and methodological differences.

Our inferred mass loading factors, $\eta_{\min} \approx (0.4\text{--}2.7) \times 10^{-2}$, are significantly lower than the predictions from high-resolution zoom-in simulations such as FIRE-2 (Pandya et al. 2021), which suggest $\eta \sim 0.3$ (and typically not exceeding 1) for galaxies with stellar masses $\log(M_\star/M_\odot) \sim 10.3$ at $z \sim 1$. Large-volume simulations such as TNG-50 (Nelson et al. 2019) and EAGLE (Mitchell et al. 2020) predict even higher mass loading factors, $\eta \sim 10$, along with outflow velocities of $\sim 400 \text{ km s}^{-1}$ and bi-conical geometries with opening angles of 40° – 50° at similar galactocentric distances. Our measurements therefore provide

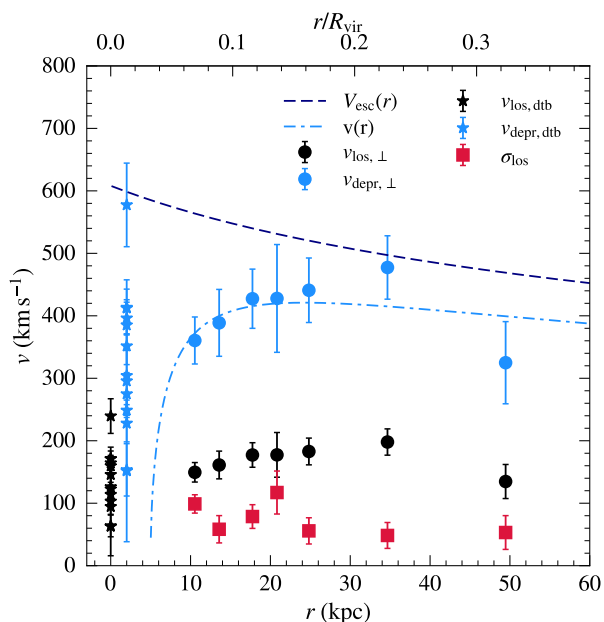


Fig. 6: Velocity profile of the Mg II-traced outflow in G1 as a function of de-projected radius. Black circles show the absolute line-of-sight velocity centroids, $|v_{\text{los},\perp}|$, measured along transverse sightlines probing the projected minor axis of G1, plotted as a function of de-projected galactocentric radius $r = \rho / \sin i$. Light-blue circles show the corresponding de-projected velocities, $v_{\text{depr},\perp} = |v_{\text{los},\perp}| / \cos i$, assuming a collimated outflow perpendicular to the disk with inclination $i = 65.5^\circ$. Red squares indicate the line-of-sight velocity dispersions along the transverse sightlines, $\sigma_{\text{los},\perp}$. Black stars at $r = 0$ show the absolute line-of-sight down-the-barrel velocities, $|v_{\text{los},\text{dtb}}|$, placed at $r = 0$ for visualization purposes only owing to the unknown physical scales probed by these sightlines; light-blue stars offset slightly in r indicate the corresponding de-projected down-the-barrel velocities, $v_{\text{depr},\text{dtb}} = |v_{\text{los},\text{dtb}}| / \cos i$. The navy dashed curve shows the escape-velocity profile $V_{\text{esc}}(r)$ (Sect. 4.2). The light-blue dash-dotted curve shows the best-fit momentum-driven wind model $v(r)$ fitted to $v_{\text{depr},\perp}$ vs. r , with best-fit parameters $r_0 = 5.25$ kpc, $v_0 = 116$ km s $^{-1}$, and $\log(N_{\text{H}}/\text{cm}^{-2}) = 19.96$. The top axis indicates the corresponding radial distance in units of the virial radius, r/R_{vir} .

conservative lower limits that are compatible with these models, but do not allow us to discriminate among them given the uncertainties in geometry, ionization corrections, and column density.

Finally, recent high-resolution simulations of galactic winds (Kim et al. 2020a,b; Schneider et al. 2020; Li & Bryan 2020) explicitly modelling the multiphase nature of outflows, indicate that most of the outflowing mass resides in cold and warm ($T \sim 10^4$ – 10^5 K), while most of the energy is carried by hot ($T \sim 10^6$ – 10^7 K) gas. Our Mg II-based measurements trace only the cool component, potentially missing a substantial (and in some models dominant) contribution from the warm and hot phases. A complete census of the mass and energy budget would require constraints on these higher-temperature components, which remain inaccessible with the current data.

7. Discussion

7.1. The smoking gun of a galactic-scale outflow

The collective kinematic signatures observed in both down-the-barrel and transverse sightlines provide compelling evidence for a large-scale, collimated outflow originating from G1. The presence of spatially coherent blue-shifted absorption along the minor axis and down-the-barrel sightlines is difficult to reconcile with alternative mechanisms (see Sect. 7.1.2). The ratio $v_{\text{los}}/\sigma_{\text{los}} \sim 2.5$ confirms that bulk motions dominate, and the low scatter in both velocity centroids and dispersions across tens of kpc suggests a high degree of coherence in the gas dynamics.

Our de-projected velocities inferred along the arc fall within the expected range for outflow velocities (Weiner 2009; Weiner et al. 2009; Martin et al. 2012; Rubin et al. 2014), and are consistent with momentum-driven wind models, which predict outflow velocities of 2 – $3 \times V_{\text{circ}}$, and close to V_{esc} (e.g., Barai et al. 2013; Katsianis et al. 2017). Our tomographic data also provide, for the first time, a direct observational characterization of the radial velocity profile of a cool outflow at kpc scales. The geometry of the background arc allows us to map $v_{\text{depr},\perp}(r)$ up to ~ 50 kpc, revealing a clear acceleration followed by possible deceleration. A simple momentum-driven cloud model (Sect. 6.3.2) seems to reproduce this behaviour: early acceleration arises from the momentum injected by the ongoing star formation, while the deceleration reflects the increasing relative influence of the galaxy’s gravitational potential. The model requires column densities of $\log(N_{\text{H}}/\text{cm}^{-2}) \approx 20$ to reproduce the measured velocities, implying that only relatively dense cool clouds can reach several tens of kiloparsecs through this mechanism. However, this column density is as seen from the galaxy radially outwards, and does not necessarily need to match the line-of-sight $N_{\text{H},1}$.

The values of $\sigma_{\text{los}} \approx 50$ – 120 km s $^{-1}$ are comparable to those seen in Mg II absorbers toward background quasars (e.g., Lan & Mo 2018), and similar to values reported in other arc-based studies (Lopez et al. 2020; Tejos et al. 2021; Mortensen et al. 2021). We remark that the observed velocity dispersions are not expected to trace the thermal broadening of the gas. Instead, they likely reflect the kinematics of ensembles of cool, coherence complexes at the kpc scales (e.g. Afruni et al. 2023; Lopez et al. 2024), that are unresolved at the spectral resolution of our observations. High-resolution observations of background quasars generally reveal the presence of multiple narrow components (e.g. Churchill & Vogt 2001), generally interpreted as discrete clumps, which are expected to be smaller than the spatial sampling of our observations of ~ 6 kpc \times 6 kpc (see e.g. Chen et al. 2014; Afruni et al. 2023). In this case, the integrated line profiles likely represent the collective motion of such clouds within each spaxel.

These σ_{los} values can be interpreted in the context of a bi-conical outflow geometry with opening angle θ_c , which naturally produces a variation in v_{los} in the range $\cos(i - \theta_c) \lesssim v_{\text{los}}/V \lesssim \cos(i + \theta_c)$ along a sightline intercepting the axis of the outflow cone given a radial velocity V and galaxy inclination i . For an opening angle $\theta_c = 17.8^\circ$ (see Sect. 6.3.1), and considering G1’s inclination, an outflow velocity of $V = 400$ km s $^{-1}$ results in a spread $\Delta v_{\text{los}} \approx 200$ km s $^{-1}$, which may explain the observed line-widths considering σ_{los} only characterizes 1σ of the full spread of v_{los} , and is expected to remain constant if V and $\theta_c \sim$ constant. Measuring an azimuthal dependence of σ_{los} within an outflow cone will be essential for confirming this projection effect.

The relatively low scatter in v_{los} and σ_{los} across tens of kpc implies a remarkable degree of kinematic coherence of the kinematics of these clouds, both in bulk velocity and integrated mo-

tions along the line of sight, further supporting the outflow interpretation if projection effects dominate σ_{los} . Taken together, the large-scale kinematic coherence, the minor-axis orientation of the sightlines, and the consistency with momentum-driven wind models strongly support a scenario in which the observed gas traces the bulk kinematics of a collimated, galactic-scale outflow, with projection effects likely dominating the observed velocity dispersions.

7.1.1. Signatures of gas recycling

Our results show that the outflow plays a key role in sustaining cool, metal-enriched gas within the CGM of G1, injecting metals out to at least $0.3 R_{\text{vir}}$. The de-projected velocities remain below the halo escape velocity, indicating that most of the ejected material is gravitationally bound and might eventually recycle back onto the galaxy. Indeed, single-sightline-probed galactic winds (Bouché et al. 2012; Schroetter et al. 2019) indicate that cool outflows traced by Mg II absorption hardly reach the escape velocities of halos for galaxies between $10 < \log(M_{\star}/M_{\odot}) < 11$. In the broader CGM context, Mg II absorption is typically concentrated within the inner halo, with the bulk of absorbers residing at $\lesssim 0.3 R_{\text{vir}}$, and with rapidly declining covering fractions beyond $\sim 0.3\text{--}0.5 R_{\text{vir}}$ (Nielsen et al. 2013b; Huang et al. 2021). Our detection of cool gas out to $0.3 R_{\text{vir}}$ therefore places G1 at the characteristic outer edge where strong Mg II-bearing clouds remain common in star-forming halos at $z \sim 1$.

The sub-escape velocities and the apparent deceleration at $\sim 0.3 R_{\text{vir}}$ suggest that the bulk of the cool outflowing gas is confined within the inner halo, where it may mix with the ambient CGM or be recycled back onto the galaxy. The suppression of Mg II absorption beyond this radius, as seen in galaxy–quasar pair studies (Churchill et al. 2013a), further supports this interpretation. However, since the deceleration in our system is inferred from a single outer sightline, additional tomographic constraints at larger impact parameters are required to confirm this behaviour in individual systems.

The presence of cool gas at $0.3 R_{\text{vir}}$ implies a travel time of ~ 100 Myr, corresponding to a recycling timescale of at least ~ 200 Myr, which is consistent with cosmological simulations predicting that most of the recycling occurs within $0.3 R_{\text{vir}}$ with median recycling timescales of 100–350 Myr at these redshifts. Assuming a constant $\dot{M}_{\text{out}} = 0.2 M_{\odot} \text{ yr}^{-1}$, which is reasonable because the UV and emission-line-based SFRs are consistent (an indicator of steady star formation in the last few hundred Myr Kennicutt & Evans 2012), we obtain a minimum processed gas mass of $0.4 \times 10^8 M_{\odot}$ stored within the CGM of G1. We emphasize that this result is based on a lower limit on \dot{M}_{out} , and that Mg II traces only the cool phase; therefore, this reservoir mass should be regarded as a lower limit to the total recycled mass in the halo.

7.1.2. Alternative scenarios

To assess whether the absorbing gas could originate from mechanisms other than outflows, we consider several alternatives. First, we disfavour ram-pressure stripping and tidal tails. G1 is isolated, with no neighbouring galaxies within 3000 km s^{-1} in redshift and $500 \text{ kpc} \times 500 \text{ kpc}$ in projected area. Moreover, tidal tails are typically narrow (A few kpc, see e.g. Bonaca et al. 2020), making it unlikely for our extended arc—spanning tens of kpc in projection—to align by chance with such a structure.

A pressure-supported CGM is also disfavoured. Although the measured σ_{los} values are comparable to the expected dark matter halo velocity dispersion of $\sigma_{\text{DM}} \approx 104 \text{ km s}^{-1}$, our data show that velocity offsets clearly dominate over the observed dispersions, with a mean ratio $v_{\text{los}}/\sigma_{\text{los}} \sim 2.5$. In a pressure-supported medium, one would instead expect dispersion-dominated kinematics with no systematic velocity shifts, whereas our measurements favour ordered bulk motions.

We further disfavour accretion in the form of an extended rotating disk. The transverse absorptions arise along the projected minor axis and exhibit kinematics inconsistent with co-planar rotation (see Sect. 4.3). A contribution from co-rotating ISM embedded within the down-the-barrel absorption cannot be completely excluded; however, isolating such a component would require higher spectral resolution and S/N.

Another interpretation is that the transverse sightlines probe radial inflows on the far side of the galaxy. While we cannot entirely rule out this possibility, down-the-barrel absorptions unambiguously indicate a galactic outflow towards the observer. Considering that v_{dib} and v_{\perp} have similar values and are both oriented along the minor axis, the simplest and most self-consistent explanation is that the transverse absorptions probe the same outflow.

7.2. Azimuthal vs. luminosity dependence on $W_r(2796)$

Several studies have found strong evidence a bi-modality in the azimuthal distribution of Mg II absorbers using both individual background sources (e.g., Kacprzak et al. 2012; Schroetter et al. 2019; Martin et al. 2019; Lundgren et al. 2021), and stacked spectroscopy (Bordoloi et al. 2011), particularly in inclined blue star-forming galaxies, and stronger Mg II equivalent widths are preferentially found along the minor axis of galaxies (Martin et al. 2019; Schroetter et al. 2019; Lundgren et al. 2021). The usual interpretation is that the bi-modality arises because of outflows and co-planar accretion in the form of extended disks, which are expected to emerge along the minor and major axes, respectively. Arc tomography results support this picture: Tejos et al. (2021) and Fernandez-Figueroa et al. (2022) identified a mild azimuthal correlation in Mg II, consistent with a composite CGM made of bi-conical outflows and extended disks, while Lopez et al. (2020) found evidence of an extended co-rotating along the major axis of their absorber galaxy (G1-0311 hereafter). In our study, our galaxy (G1-0224, for the following discussion) is probed predominantly along the minor axis, where we found strong evidence for the presence of an outflow. Although our transverse sightlines do not sample the full range of azimuthal angles, the fact that G1-0224 and G1-0311 are probed close to the minor and major axes, respectively, provides a useful comparison to assess how $W_r(2796)$ varies with geometry.

Despite their different orientations, both systems show low intrinsic scatter in their individual $W_r\text{--}\rho$ relations, indicating coherent cool gas structures over scales of tens of kpc. When considered together, however, they span much of the scatter seen in quasar-based Mg II samples (Fig. 5, panel b). Importantly, the two galaxies differ substantially in M_{\star} , M_B , and SFR: G1-0224 is ~ 4 times more massive and ~ 20 times more luminous in B-band than G1-0311, which is transitioning toward quiescence.

The Mg II absorption is well-established to strongly correlate with host galaxy properties such as stellar mass and luminosity (e.g., Chen & Tinker 2008; Chen et al. 2010; Bordoloi et al. 2011). Chen et al. (2010) showed that much of the $W_r\text{--}\rho$ scatter can be reduced by scaling the impact parameters with B-band luminosity:

$$\log \rho_{L_*} = \log \rho \times (L_B/L_{B_*})^{-0.35} \quad (2)$$

implying that the extent of the cool, Mg II-bearing CGM grows with galaxy luminosity. This is one manifestation of the self-similar CGM proposed by Churchill et al. (2013b), in which galaxies of different luminosities and masses follow a common W_r –(ρ/R_{vir}) relation.

To disentangle the effects of azimuth and luminosity on W_r (2796), we calculated partial Spearman rank correlations while accounting for the natural degeneracy between ϕ and ρ introduced by the arc geometries. Considering both G1-0224 and G1-0311, we find a strong anti-correlation between W_r (2796) and ρ (Spearman rank correlation coefficient r_S and associated p -value; $r_S = -0.83$, $p = 9 \times 10^{-6}$), as expected from quasar-based studies (Nielsen et al. 2013b; Huang et al. 2021), but only a moderate but statistically significant correlation with ϕ ($r_S = 0.65$, $p = 0.002$). Scaling ρ using Eq. 2 weakens the W_r (2796)– ϕ correlation ($r_S = 0.31$, $p = 0.18$), whereas the W_r – ρ_{L_*} remains highly significant ($r_S = -0.87$, $p = 10^{-6}$). A multivariate Energy Test shows that the original W_r – ρ distributions of the two galaxies differ ($p = 0.03$), but become statistically consistent after luminosity scaling ($p = 0.22$). This confirms that B-band luminosity reduces the scatter in the W_r – ρ relation, implying that part of the large dispersion in quasar absorber statistics has an important contribution from the heterogeneity of the galaxy population, and also that the W_r – ρ anti-correlation has a similar shape along both major and minor axis directions once host properties are accounted for.

This result must be interpreted with care. The apparent similarity of the W_r – ρ profiles for G1-0224 and G1-0311 does not contradict the well-established azimuthal trends derived from large Mg II absorber samples, which demonstrate a statistical excess of absorbers along galaxy minor axes. Instead, our analysis shows that in two well-characterised halos—one probed near the minor axis (G1-0224) and the other near the major axis (G1-0311)—the W_r – ρ relations are essentially indistinguishable once scaled by host luminosity (and therefore indirectly by halo mass/size). Despite sampling geometries traditionally associated with different physical processes (outflows along the minor axis vs. extended disks/inflows along the major axis), the cool gas absorption strength declines with radius in nearly the same way in these two systems. This does not refute the existence of azimuthal bi-modality; rather, it shows that projected geometry alone does not guarantee a significant difference in W_r at fixed ρ . Host galaxy properties—such as luminosity, stellar mass, and star-formation rate—may exert a stronger influence on the absorber strength than the projected orientation of the sightlines. Determining whether this is a general feature of individual systems or specific to the particular evolutionary states of G1-0224 and G1-0311, will require a larger sample of arc tomography systems.

8. Summary and conclusions

We have conducted a spatially resolved study of the cool CGM surrounding G1, a luminous ($2.6 L_B^*$), star-forming (SFR $\approx 15 M_\odot \text{ yr}^{-1}$), and relatively massive ($\log(M_*/M_\odot) \approx 10.3$) main-sequence galaxy at $z \sim 1$. The fortuitous alignment of a background gravitational arc enabled us to probe metal absorption from the CGM of G1 in both down-the-barrel and transverse sightlines, spanning projected distances from the galactic centre out to ~ 50 kpc along the minor axis. This unique configuration revealed a galactic-scale outflow emerging along the minor

axis of G1, allowing us to characterize its geometry and kinematics with unprecedented spatial resolution for absorption-line studies. Our main findings are summarized as follows:

- (I) Spatially coherent, blue-shifted metal absorption lines detected along the minor axis of a star-forming galaxy, extending out to projected distances of ~ 50 kpc, provide strong evidence for the detection of a large-scale outflow traced in absorption using gravitational-arc tomography.
- (II) The data disfavours a spherical or isotropic outflow geometry, and instead, support a collimated wind emerging along the minor axis with opening angle $\sim 18^\circ$ – 25° , minimum mass outflow rates $\dot{M}_{\text{min, out}} \sim 0.06$ – $0.4 M_\odot \text{ yr}^{-1}$, and mass loading factor of $\eta_{\text{min}} \sim 0.004$ – 0.027 , measured within projected distances of 10–50 kpc. These values are broadly consistent with expectations from cosmological simulations.
- (III) The transverse and down-the-barrel absorptions show strong blueshifts, with values up to $\sim 240 \text{ km s}^{-1}$. Combined with relatively low σ_{los} values, this implies that the gas is dominated by bulk motion ($v_{\text{los}}/\sigma_{\text{los}} \sim 2.5$). The small scatter in v_{los} and σ_{los} points to high kinematic coherence over tens of kpc.
- (IV) A momentum-driven wind model appears to describe the radial profile of the outflowing cool gas. An initial acceleration of $v_{\text{depr, \perp}}$ can be explained by momentum injection from the star-formation, and a subsequent deceleration dominated by the gravitational potential. Both the measured $v_{\text{depr, \perp}}$ values and the momentum-driven cloud model indicate that the gas barely reaches the escape velocity of the halo, and is likely to be retained within the halo. We estimate a recycling timescale of ~ 200 Myr, implying a minimum processed gas mass of $0.4 \times 10^8 M_\odot$, in the CGM of G1, within $0.3 R_{\text{vir}}$.
- (V) Our measurements of W_r (2796) are statistically consistent with the canonical W_r – ρ anti-correlation established from quasar-galaxy pairs. Notably, the scatter in our measurements is small and comparable to that in previous arc tomography studies, supporting the scenario that a significant fraction of the scatter in the quasar statistics is driven by heterogeneity in the host-galaxy properties.
- (VI) Compared with a previously studied arc system probing the major axis (Lopez et al. 2020), our minor-axis sightlines yield systematically higher W_r (2796) values. However, once the impact parameters are scaled by the B-band luminosity of the host galaxy, this difference diminishes, and the W_r – ρ distributions become statistically consistent, indicating that major/minor axis alignment does not necessarily guarantee smaller/larger W_r (2796) after accounting for host-galaxy properties.

Our findings provide direct evidence for the physical connection between galactic outflows and the cool, metal-bearing CGM. By resolving its structure and kinematics across tens of kpc, we offer new constraints on the geometry, extent, and kinematics of feedback-driven winds.

Acknowledgements. We thank the anonymous referee for constructive comments and suggestions that significantly improved the clarity and quality of the manuscript. S.L. and N.T. acknowledge support by FONDECYT grant 1231187. J.H. acknowledges support from Beca ANID Doctorado Nacional Folio 21230522. J.H. and L.F.B. acknowledge support from ANID BASAL project FB210003, FONDECYT projects 1230231, and CASSACA project CCJRF1906. Based on observations collected at the European Southern Observatory under ESO programme 094.A-0141 (PI: SWINBANK). This research is partly based on observations made with the NASA/ESA Hubble Space Telescope obtained from the Space Telescope Science Institute, which is operated by

the Association of Universities for Research in Astronomy, Inc., under NASA contract NAS 5–26555. These observations are associated with program GO 14497 (PI Smit), and GO 9135 (PI Gladders). This research has made use of the Astrophysics Data System, funded by NASA under Cooperative Agreement 80NSSC21M00561. This work made use of Astropy:¹ a community-developed core Python package and an ecosystem of tools and resources for astronomy. This work also thanks contributors to GalPak^{3D}², MPAF³, BAGPIPES⁴, NumPy⁵, SciPy⁶, Matplotlib⁷ LINETOOLS⁸, the PYTHON programming language⁹, and the free and open-source community.

References

- Afruni, A., Fraternali, F., & Pezzulli, G. 2021, *MNRAS*, 501, 5575
- Afruni, A., Lopez, S., Anshul, P., et al. 2023, *A&A*, 680, A112
- Anand, G. S., Mack, J., Avila, R. J., et al. 2025, in *The DrizzlePac Handbook*, 3
- Astropy Collaboration, Price-Whelan, A. M., Lim, P. L., et al. 2022, *ApJ*, 935, 167
- Astropy Collaboration, Price-Whelan, A. M., Sipőcz, B. M., et al. 2018, *AJ*, 156, 123
- Astropy Collaboration, Robitaille, T. P., Tollerud, E. J., et al. 2013, *A&A*, 558, A33
- Bacon, R., Accardo, M., Adjali, L., et al. 2010, in *SPIE Conference Series*, Vol. 7735, , 773508
- Bacon, R., Piqueras, L., Conseil, S., Richard, J., & Shepherd, M. 2016, *MPDAF: MUSE Python Data Analysis Framework*, Astrophysics Source Code Library, record ascl:1611.003
- Barai, P., Viel, M., Borgani, S., et al. 2013, *MNRAS*, 430, 3213
- Berg, T. A. M., Afruni, A., Ledoux, C., et al. 2025, *A&A*, 693, A200
- Bergeron, J. & Stasińska, G. 1986, *A&A*, 169, 1
- Bertin, E. & Arnouts, S. 1996, *A&AS*, 117, 393
- Bonaca, A., Pearson, S., Price-Whelan, A. M., et al. 2020, *ApJ*, 889, 70
- Bordoloi, R., Lilly, S. J., Knobel, C., et al. 2011, *ApJ*, 743, 10
- Bouché, N., Carfantan, H., Schroetter, I., Michel-Dansac, L., & Contini, T. 2015
- Bouché, N., Hohensee, W., Vargas, R., et al. 2012, *MNRAS*, 426, 801
- Burchett, J. N., Rubin, K. H. R., Prochaska, J. X., et al. 2021, *ApJ*, 909, 151
- Carnall, A. C., McLure, R. J., Dunlop, J. S., et al. 2019, *MNRAS*, 490, 417
- Carnall, A. C., McLure, R. J., Dunlop, J. S., & Davé, R. 2018, *MNRAS*, 480, 4379
- Charlot, S. & Fall, S. M. 2000, *ApJ*, 539, 718
- Chen, H.-W., Gauthier, J.-R., Sharon, K., et al. 2014, *MNRAS*, 438, 1435
- Chen, H.-W., Helsby, J. E., Gauthier, J.-R., et al. 2010, *ApJ*, 714, 1521
- Chen, H.-W. & Tinker, J. L. 2008, *ApJ*, 687, 745
- Child, H. L., Habib, S., Heitmann, K., et al. 2018, *ApJ*, 859, 55
- Churchill, C. W., Nielsen, N. M., Kacprzak, G. G., & Trujillo-Gomez, S. 2013a, *ApJ*, 763, L42
- Churchill, C. W., Steidel, C. C., & Vogt, S. S. 1996, *ApJ*, 471, 164
- Churchill, C. W., Trujillo-Gomez, S., Nielsen, N. M., & Kacprzak, G. G. 2013b, *ApJ*, 779, 87
- Churchill, C. W. & Vogt, S. S. 2001, *AJ*, 122, 679
- Coil, A. L., Weiner, B. J., Holz, D. E., et al. 2011, *ApJ*, 743, 46
- Draine, B. T. 2011, *Physics of the Interstellar and Intergalactic Medium*
- Dutta, R., Fumagalli, M., Fossati, M., et al. 2020, *MNRAS*, 499, 5022
- Elahi, P. J., Power, C., Lagos, C. d. P., Poulton, R., & Robotham, A. S. G. 2018, *MNRAS*, 477, 616
- Elmegreen, D. M., Elmegreen, B. G., Rubin, D. S., & Schaffer, M. A. 2005, *ApJ*, 631, 85
- ESO CPL Development Team. 2015, *EsoRex: ESO Recipe Execution Tool*, Astrophysics Source Code Library
- Faucher-Giguère, C.-A. & Oh, S. P. 2023, *ARA&A*, 61, 131
- Fernandez-Figueroa, A., Lopez, S., Tejos, N., et al. 2022, *MNRAS*, 517, 2214
- Fitzpatrick, E. L. 1999, *PASP*, 111, 63
- Förster Schreiber, N. M., Genzel, R., Bouché, N., et al. 2009, *ApJ*, 706, 1364
- Gauthier, J.-R. & Chen, H.-W. 2012, *MNRAS*, 424, 1952
- Gladders, M. D., Yee, H. K. C., & Ellingson, E. 2002, *AJ*, 123, 1
- Guérou, A., Krajinović, D., Epinat, B., et al. 2017, *A&A*, 608, A5
- Guo, Y., Ferguson, H. C., Bell, E. F., et al. 2015, *ApJ*, 800, 39
- Harris, C. R., Millman, K. J., van der Walt, S. J., et al. 2020, *Nature*, 585, 357
- Heckman, T. M., Alexandroff, R. M., Borthakur, S., Overzier, R., & Leitherer, C. 2015, *ApJ*, 809, 147
- Ho, S. H., Martin, C. L., Kacprzak, G. G., & Churchill, C. W. 2017, *ApJ*, 835, 267
- Huang, Y.-H., Chen, H.-W., Shectman, S. A., et al. 2021, *MNRAS*, 502, 4743
- Hunter, J. D. 2007, *Computing in Science & Engineering*, 9, 90
- Jenkins, E. B. 2009, *ApJ*, 700, 1299
- Jullo, E., Kneib, J. P., Limousin, M., et al. 2007, *New Journal of Physics*, 9, 447
- Kacprzak, G. G., Churchill, C. W., & Nielsen, N. M. 2012, *ApJ*, 760, L7
- Kacprzak, G. G., Martin, C. L., Bouché, N., et al. 2014, *ApJ*, 792, L12
- Kalita, B. S., Suzuki, T. L., Kashino, D., et al. 2025, *MNRAS*, 536, 3090
- Katsianis, A., Tesfari, E., Blanc, G., & Sargent, M. 2017, *MNRAS*, 464, 4977
- Kennicutt, Robert C., J. 1998, *ARA&A*, 36, 189
- Kennicutt, R. C. & Evans, N. J. 2012, *ARA&A*, 50, 531
- Kim, C.-G., Ostriker, E. C., Fielding, D. B., et al. 2020a, *ApJ*, 903, L34
- Kim, C.-G., Ostriker, E. C., Somerville, R. S., et al. 2020b, *ApJ*, 900, 61
- Lan, T.-W. & Fukugita, M. 2017, *ApJ*, 850, 156
- Lan, T.-W. & Mo, H. 2018, *ApJ*, 866, 36
- Lanzetta, K. M., Wolfe, A. M., Turnshek, D. A., et al. 1991, *ApJS*, 77, 1
- Law, D. R., Steidel, C. C., Erb, D. K., et al. 2007, *ApJ*, 656, 1
- Li, M. & Bryan, G. L. 2020, *ApJ*, 890, L30
- Lopez, S., Afruni, A., Zamora, D., et al. 2024, *A&A*, 691, A356
- Lopez, S. & Krogager, J.-K. 2025, *A&A*, 703, A21
- Lopez, S., Tejos, N., Barrientos, L. F., et al. 2020, *MNRAS*, 491, 4442
- Lopez, S., Tejos, N., Ledoux, C., et al. 2018, *Nature*, 554, 493
- Lundgren, B. F., Creech, S., Brammer, G., et al. 2021, *ApJ*, 913, 50
- Martin, C. L. 2005, *ApJ*, 621, 227
- Martin, C. L. & Bouché, N. 2009, *ApJ*, 703, 1394
- Martin, C. L., Ho, S. H., Kacprzak, G. G., & Churchill, C. W. 2019, *ApJ*, 878, 84
- Martin, C. L., Shapley, A. E., Coil, A. L., et al. 2012, *ApJ*, 760, 127
- Matejek, M. S. & Simcoe, R. A. 2012, *ApJ*, 761, 112
- Ménard, B. & Chelouche, D. 2009, *MNRAS*, 393, 808
- Mitchell, P. D., Schaye, J., Bower, R. G., & Crain, R. A. 2020, *MNRAS*, 494, 3971
- Mortensen, K., Keerthi Vasan, G. C., Jones, T., et al. 2021, *ApJ*, 914, 92
- Moster, B. P., Somerville, R. S., Maubetsch, C., et al. 2010, *ApJ*, 710, 903
- Murray, N., Quataert, E., & Thompson, T. A. 2005, *ApJ*, 618, 569
- Navarro, J. F., Frenk, C. S., & White, S. D. M. 1996, *ApJ*, 462, 563
- Nelson, D., Pillepich, A., Springel, V., et al. 2019, *MNRAS*, 490, 3234
- Nielsen, N. M., Churchill, C. W., & Kacprzak, G. G. 2013a, *ApJ*, 776, 115
- Nielsen, N. M., Churchill, C. W., Kacprzak, G. G., & Murphy, M. T. 2013b, *ApJ*, 776, 114
- Nielsen, N. M., Fisher, D. B., Kacprzak, G. G., et al. 2024, *Nature Astronomy*, 8, 1602
- Pandya, V., Fielding, D. B., Anglés-Alcázar, D., et al. 2021, *MNRAS*, 508, 2979
- Patrício, V., Richard, J., Carton, D., et al. 2018, *MNRAS*, 477, 18
- Peng, C. Y., Ho, L. C., Impey, C. D., & Rix, H.-W. 2002, *AJ*, 124, 266
- Péroux, C. & Howk, J. C. 2020, *ARA&A*, 58, 363
- Pessa, I., Wisotzki, L., Urrutia, T., et al. 2024, *A&A*, 691, A5
- Popesso, P., Concas, A., Cresci, G., et al. 2023, *MNRAS*, 519, 1526
- Prochaska, J. X., Tejos, N., Crighton, N., et al. 2017, *linetools/linetools: Third Minor Release*
- Rubin, K. H. R., Diamond-Stanic, A. M., Coil, A. L., Crighton, N. H. M., & Stewart, K. R. 2018, *ApJ*, 868, 142
- Rubin, K. H. R., Prochaska, J. X., Koo, D. C., et al. 2014, *ApJ*, 794, 156
- Rubin, K. H. R., Prochaska, J. X., Ménard, B., et al. 2011, *ApJ*, 728, 55
- Rubin, K. H. R., Weiner, B. J., Koo, D. C., et al. 2010, *ApJ*, 719, 1503
- Rupke, D. S., Veilleux, S., & Sanders, D. B. 2005, *ApJS*, 160, 115
- Savage, B. D. & Sembach, K. R. 1996, *ARA&A*, 34, 279
- Schlafly, E. F. & Finkbeiner, D. P. 2011, *ApJ*, 737, 103
- Schlegel, D. J., Finkbeiner, D. P., & Davis, M. 1998, *ApJ*, 500, 525
- Schneider, E. E., Ostriker, E. C., Robertson, B. E., & Thompson, T. A. 2020, *ApJ*, 895, 43
- Schroetter, I., Bouché, N., Wendt, M., et al. 2016, *ApJ*, 833, 39
- Schroetter, I., Bouché, N. F., Zabl, J., et al. 2019, *MNRAS*, 490, 4368
- Shaban, A., Bordoloi, R., O'Meara, J. M., et al. 2025, *ApJ*, 986, 190
- Shibuya, T., Ouchi, M., Kubo, M., & Harikane, Y. 2016, *ApJ*, 821, 72
- Smit, R., Swinbank, A. M., Massey, R., et al. 2017, *MNRAS*, 467, 3306
- Soto, K. T., Lilly, S. J., Bacon, R., Richard, J., & Conseil, S. 2016, *MNRAS*, 458, 3210
- Steidel, C. C. 1995, in *QSO Absorption Lines*, ed. G. Meylan, 139
- Swinbank, A. M., Bower, R. G., Smith, G. P., et al. 2007, *MNRAS*, 376, 479
- Tejos, N., López, S., Ledoux, C., et al. 2021, *MNRAS*, 507, 663
- Tremonti, C. A., Moustakas, J., & Diamond-Stanic, A. M. 2007, *ApJ*, 663, L77
- Tumlinson, J., Peebles, M. S., & Werk, J. K. 2017, *ARA&A*, 55, 389
- Veilleux, S., Maiolino, R., Bolatto, A. D., & Aalto, S. 2020, *A&A Rev.*, 28, 2
- Virtanen, P., Gommers, R., Oliphant, T. E., et al. 2020, *Nature Methods*, 17, 261
- Weillbacher, P. M., Streicher, O., Urrutia, T., et al. 2012, in *Proc. SPIE*, Vol. 8451, Software and Cyberinfrastructure for Astronomy II, 84510B
- Weiner, B. J. 2009, in *American Institute of Physics Conference Series*, Vol. 1201, *The Monster's Fiery Breath: Feedback in Galaxies, Groups, and Clusters*, ed. S. Heinz & E. Wilcots (AIP), 142–145
- Weiner, B. J., Coil, A. L., Prochaska, J. X., et al. 2009, *ApJ*, 692, 187
- Willmer, C. N. A., Faber, S. M., Koo, D. C., et al. 2006, *ApJ*, 647, 853
- Zabl, J., Bouché, N. F., Schroetter, I., et al. 2020, *MNRAS*, 492, 4576
- Zabl, J., Bouché, N. F., Schroetter, I., et al. 2019, *MNRAS*, 485, 1961

Appendix A: Strong lens modelling

We used the publicly available software LENSTOOL (Jullo et al. 2007) to perform parametric modelling of the cluster mass distribution. The model includes a large-scale smooth component representing the cluster’s dark matter halo and individual mass components associated with cluster galaxies. The mass distributions of both cluster-scale and galaxy-scale halos were modelled as truncated pseudo-isothermal elliptical mass distributions (PIEMDs). For the cluster-scale halo, we adopted a PIEMD potential centred around the brightest cluster galaxy (BCG) at $z_{\text{cluster}} = 0.773$. All model parameters—position, velocity dispersion, ellipticity, and position angle—were allowed to vary with broad priors, except for the cut radius, which was fixed to 1000 kpc, well beyond the strong-lensing regime. For the galaxy-scale halos, we included sixteen spectroscopically confirmed cluster members detected in the MUSE data. These galaxies were selected to be within $\pm 3000 \text{ km s}^{-1}$, of the cluster redshift, and within $30''$ of the BCG, where strong-lensing constraints are available.

Photometric and morphological properties of the cluster galaxies were measured using SExtractor (Bertin & Arnouts 1996) in the *HST* imaging. We fixed their centroids, position angles, and ellipticities according to their morphology measured by SExtractor. We scaled their velocity dispersions (σ_{LENSTOOL}), core (r_{core}), and cut radius (r_{cut}) adopting the scaling relations detailed in Jullo et al. (2007). A reference luminosity L_* was chosen for a galaxy with apparent magnitude $m_{\text{F160W}} = 18$. The reference core radius r_{core}^* was fixed to a negligible but non-zero value.

The best-fit parameters for the cluster-scale halo are a velocity dispersion $\sigma_{\text{LENSTOOL}} = 632 \pm 45 \text{ km s}^{-1}$, an ellipticity of 0.65 ± 0.1 with a position angle of $45 \pm 1.5^\circ$, and a core radius of $r_{\text{core}} = 6.8 \pm 10 \text{ kpc}$. For a cluster galaxy with reference magnitude $m_{\text{F160W}} = 18$, we obtained a best-fit velocity dispersion $\sigma_{\text{LENSTOOL}} = 359 \pm 68 \text{ km s}^{-1}$ and cut radius $r_{\text{cut}} = 46.2 \pm 64 \text{ kpc}$. This model achieves an image-plane RMS of $0.79''$, with a $\chi^2 = 13.7$ with 11 free parameters.

Appendix B: SED modelling and halo properties

We first modelled the spectral energy distribution (SED) of G1 using BAGPIPES (Carnall et al. 2018, Carnall et al. 2019), jointly fitting its MUSE and *HST* photometry. The MUSE spectrum of G1 was extracted on a $1.5''$ aperture on the MUSE data, corrected for both lensing magnification and Galactic extinction (using the same procedure as in Sect. 4.1), which is shown in Fig. D.1.

For the SED model, we assumed a double power law for the star formation history (SFH), and the Charlot & Fall (2000) extinction law (CF00), with uniform priors of $0 < A_V < 2$ and $-4 < n < 4$ for the dust attenuation. A nebular component is included with ionization parameter $-3 \leq \log U \leq -2$. We adopt uniform priors for the stellar velocity dispersion ($50 \text{ km s}^{-1} < \sigma < 300 \text{ km s}^{-1}$), and metallicity ($0.2 < [Z/H] < 4$). The resulting stellar mass and SFR were inferred from the posterior distributions and are listed in Table 1.

Next, we estimate the halo mass M_h using the stellar-mass-halo-mass (SMHM) relation from Moster et al. (2010), assuming $M_h = M_{200}$. From this, we derived the virial radius via $R_{\text{vir}} = [3M_h/(4\pi 200\rho_c(z))]^{1/3}$ and the maximum circular velocity as $V_{\text{max}} = [10M_hGH(z)]^{1/3}$, where G is the gravitational constant, and $\rho_c(z)$ and $H(z)$ are the critical density and Hubble parameter at redshift z . The halo velocity dispersion was

estimated using the scaling relation from Elahi et al. (2018): $\sigma_{\text{DM}} \simeq 430 (M_h/10^{14} M_\odot)^{1/3} \text{ km s}^{-1}$.

We estimated the escape velocity $V_{\text{esc}}(r) = \sqrt{2|\phi(r)|}$ and circular velocity $V_{\text{circ}}(r) = \sqrt{r|d\phi(r)/dr|}$ for G1, assuming a Navarro-Frenk-White (Navarro et al. 1996) gravitational potential $\phi(r)$ for the dark-matter (DM) halo, with concentration parameter of 5 (for galaxies with similar M_{200} from N-body simulations; Child et al. 2018). Maximum circular velocity, and escape velocities at $r = 10 \text{ kpc}$ and $r = 50 \text{ kpc}$ are indicated in Table 1.

Appendix C: Estimation of $N_{\text{H I}}$

A column density N of an absorbing species, in the optically thin regime, can be estimated as

$$N > 1.130 \times 10^{12} \text{ cm}^{-2} \frac{W_r}{f\lambda^2} \quad (\text{C.1})$$

for a given transition, where f , λ and W_r , are its oscillator strength, rest-frame wavelength, and measured rest equivalent width, respectively (Draine 2011). Although the Mg II absorption is likely saturated and unresolved, we adopt the optically thin limit to estimate a conservative lower bound on the column density. Any degree of saturation or unresolved component structure increases the true N above the linear-regime value, making the optically thin approximation a strict lower limit. For $W_r(2796) \sim 1-1.5 \text{ \AA}$ we estimate $\log(N_{\text{Mg II}}/\text{cm}^{-2}) > 13.4-13.6$.

Following Rubin et al. (2014), the corresponding $N_{\text{Mg II}}$ can be used to estimate $N_{\text{H I}}$ as:

$$N_{\text{H I}} > \frac{10^{19.3} \text{ cm}^{-2}}{\chi(\text{Mg II})} \frac{N_{\text{Mg II}}}{10^{14.4} \text{ cm}^{-2}} \frac{10^{-4.42}}{10^{\log \text{Mg/H}}} \frac{10^{-0.5}}{10^{d(\text{Mg})}} \quad (\text{C.2})$$

Assuming a solar abundance ratio $\log \text{Mg/H} = -4.42$ (Savage & Sembach 1996), unity ionization fraction $\chi(\text{Mg II}) = 1$, and dust depletion factor $d(\text{Mg}) = -0.5$ (Galactic ISM values range between -0.3 and -1.5 Jenkins 2009), we get lower limits of $\log(N_{\text{H I}}/\text{cm}^{-2}) > 18.3-18.5$.

Self-shielding is required to retain significant amounts of Mg II in dense clouds. Photoionization models show that Mg II with $\log(N_{\text{Mg II}}/\text{cm}^{-2}) \geq 13.4$ can only survive in gas with $\log(N_{\text{H I}}/\text{cm}^{-2}) \geq 18$ (Bergeron & Stasińska 1986). Moreover, empirical $W_r(2796)$ - $N_{\text{H I}}$ relations at $0.4 \lesssim z \lesssim 2.5$ based on quasar sightlines (Ménard & Chelouche 2009; Lan & Fukugita 2017) indicate that $\log(N_{\text{H I}}/\text{cm}^{-2})$ correlates with $W_r(2796)$, albeit with large scatter, however absorbers with $W_r(2796)$ between $\sim 1-1.5 \text{ \AA}$ span a around three orders of magnitude in $\log(N_{\text{H I}}/\text{cm}^{-2})$, between 18.3 and 21.6. The inferred values are consistent with the spread in $N_{\text{H I}}$ from background quasars, and the minimum $N_{\text{H I}}$ required for self-shielded clouds. We remark that, given our assumptions for saturation, abundance, ionization fraction, and dust depletion, our $N_{\text{H I}}$ lower limit estimated Eq. C.2 is extremely conservative, and a direct measurement would almost certainly yield substantially higher column densities.

Appendix D: G1 spectrum

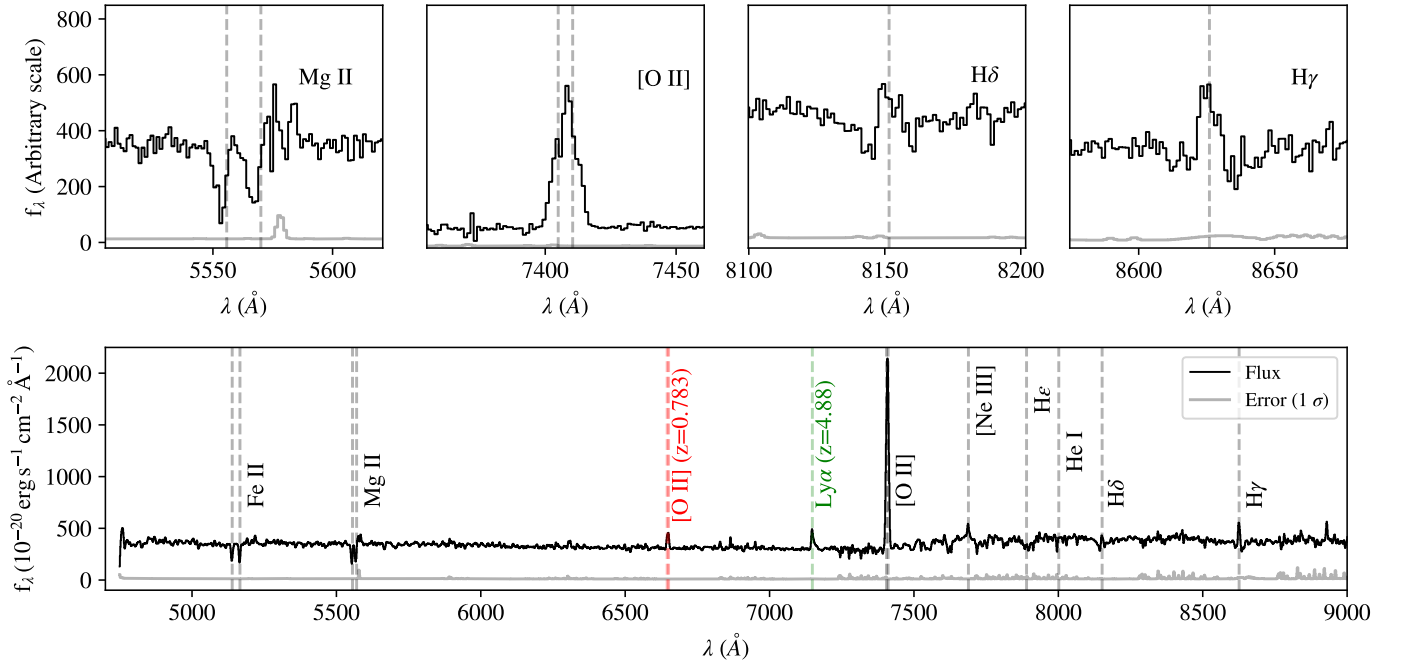


Fig. D.1: *Bottom*: Integrated MUSE spectrum of G1, corrected by Galactic extinction and lensing magnification. Vertical grey dashed lines mark the positions of strong absorption and emission features at z_{G1} . Several narrow emission lines are present, including [O II], Ne III, He I, and Balmer lines. Mg II is blue-shifted with respect to the emission lines. Ly α emission is observed at $z \sim 4.88$, corresponding to a counter-image of the arc A, and diffuse [O II] emission from the galaxy cluster at ~ 0.773 are also present in the spectrum. *Top*: From left to right, zoom-in to Mg II, [O II], H δ , and H γ lines.

Appendix E: Spatially resolved absorption-line measurements

Table E.1: Properties of the absorptions measured on the binned MUSE spaxels.

x (pix) (0)	y (pix) (1)	ρ (kpc) (2)	v_{los} (km s^{-1}) (3)	σ_{los} (km s^{-1}) (4)	ϕ (deg) (5)	W_{2586} (\AA) (6)	W_{2600} (\AA) (7)	W_{2796} (\AA) (8)	W_{2803} (\AA) (9)	$\mathcal{R}_{\text{Mg II}}^{\text{Fe II}}$ dimensionless (10)
46	31	13.3	175	< 0.88	< 0.88	< 1.05	< 1.36	...
46	32	10.1	-239 ± 27	92 ± 26	169	1.21 ± 0.38	1.21 ± 0.35	0.78 ± 0.34	< 1.11	1.55 ± 0.81
46	33	9.0	-171 ± 18	108 ± 17	141	1.68 ± 0.37	1.77 ± 0.29	2.13 ± 0.39	1.62 ± 0.55	0.83 ± 0.20
47	31	9.0	-62 ± 47	179 ± 42	-173	1.63 ± 0.55	1.89 ± 0.42	1.23 ± 0.51	< 1.23	1.54 ± 0.72
47	32	6.0	-164 ± 10	64 ± 10	166	1.20 ± 0.24	1.43 ± 0.70	1.62 ± 0.24	< 1.12	0.88 ± 0.45
47	33	4.1	-170 ± 12	109 ± 11	118	1.89 ± 0.27	2.71 ± 1.38	1.75 ± 0.28	< 0.95	1.55 ± 0.82
47	34	6.7	73	< 0.73	< 0.91	< 1.39	< 1.68	...
48	30	10.2	-159 ± 16	0 ± 63	-141	< 0.93	1.11 ± 0.36	1.03 ± 0.36	0.87 ± 0.37	1.08 ± 0.51
48	31	5.3	-145 ± 12	82 ± 11	-139	1.50 ± 0.30	1.93 ± 0.95	1.88 ± 0.28	1.31 ± 0.38	1.03 ± 0.53
48	32	1.0	-103 ± 10	98 ± 9	-105	1.64 ± 0.23	1.97 ± 0.19	2.14 ± 0.24	1.81 ± 0.42	0.92 ± 0.14
48	33	3.7	-113 ± 14	133 ± 13	21	1.73 ± 0.26	< 0.69	1.96 ± 0.27	1.84 ± 0.70	< 0.18
48	34	8.1	-126 ± 27	121 ± 26	28	1.49 ± 0.44	1.55 ± 0.66	1.51 ± 0.42	< 1.14	1.03 ± 0.53
49	31	5.5	-122 ± 22	68 ± 21	-79	< 0.66	1.43 ± 0.45	1.18 ± 0.38	< 1.28	1.20 ± 0.55
49	32	5.8	-94 ± 12	53 ± 11	-30	1.46 ± 0.30	1.51 ± 0.41	1.49 ± 0.30	1.18 ± 0.31	1.01 ± 0.34
49	33	8.8	-63 ± 17	67 ± 16	-5	1.06 ± 0.30	1.35 ± 0.27	1.05 ± 0.30	1.04 ± 0.44	1.29 ± 0.45
49	34	12.4	6	< 0.95	< 0.77	< 0.80	< 1.08	...
44	39	32.0	82	< 0.80	< 0.89	< 0.81	< 1.46	...
44	40	33.4	80	< 1.05	< 0.88	< 1.05	< 1.09	...
45	34	14.6	124	< 0.89	< 0.99	< 0.88	< 1.56	...
45	35	16.2	-177 ± 19	78 ± 18	107	0.90 ± 0.40	1.70 ± 0.70	1.57 ± 0.40	< 1.46	1.08 ± 0.52
45	36	18.9	-177 ± 35	117 ± 34	93	1.23 ± 0.54	< 0.76	1.50 ± 0.50	< 2.25	< 0.25
45	37	22.6	-182 ± 21	55 ± 20	84	< 0.91	1.00 ± 0.38	1.51 ± 0.41	0.97 ± 0.40	0.67 ± 0.31
45	38	26.9	78	< 0.83	< 0.96	< 0.78	< 0.94	...
45	39	31.5	-197 ± 21	48 ± 20	75	< 0.73	< 0.81	1.02 ± 0.30	0.97 ± 0.26	< 0.39
45	40	30.7	74	< 1.45	< 1.20	< 0.86	< 0.93	...
45	43	45.0	-134 ± 27	53 ± 27	70	< 0.79	0.74 ± 0.37	0.94 ± 0.38	< 1.04	0.79 ± 0.51
46	34	9.6	-149 ± 15	98 ± 14	109	2.08 ± 0.39	< 0.77	1.40 ± 0.35	1.39 ± 0.26	< 0.27
46	35	12.4	-161 ± 22	58 ± 21	87	< 0.78	1.19 ± 0.44	1.39 ± 0.43	< 1.58	0.86 ± 0.41
46	40	30.3	61	< 1.10	< 1.03	< 0.76	< 0.82	...

Notes.

- ⁽⁰⁾ x coordinate of the binned spaxel.
- ⁽¹⁾ y coordinate of the binned spaxel.
- ⁽²⁾ Impact parameter; projected physical separation between the centre of the spaxel and the centre of G1, in the absorber plane.
- ⁽³⁾ Line-of-sight velocity of the absorption centroid with respect to z_{G1} .
- ⁽⁴⁾ Line-of-sight velocity dispersion after subtracting the instrumental line spread function.^a
- ⁽⁵⁾ Azimuthal angle of the centre of the spaxel with respect to G1 receding major axis.
- ⁽⁶⁾ Fe II 2586 \AA rest-frame equivalent width.^b
- ⁽⁷⁾ Fe II 2600 \AA rest-frame equivalent width.^b
- ⁽⁸⁾ Mg II 2796 \AA rest-frame equivalent width.^b
- ⁽⁹⁾ Mg II 2803 \AA rest-frame equivalent width.^b
- ⁽¹⁰⁾ Ratio between $W_r(2600)$ and $W_r(2796)$.
- ^(a) The value is set to 0 when the observed FWHM is larger than the instrumental FWHM.
- ^(b) Non-detections are reported as 2σ upper limits.

Appendix F: Spatial distribution of Mg II spectra

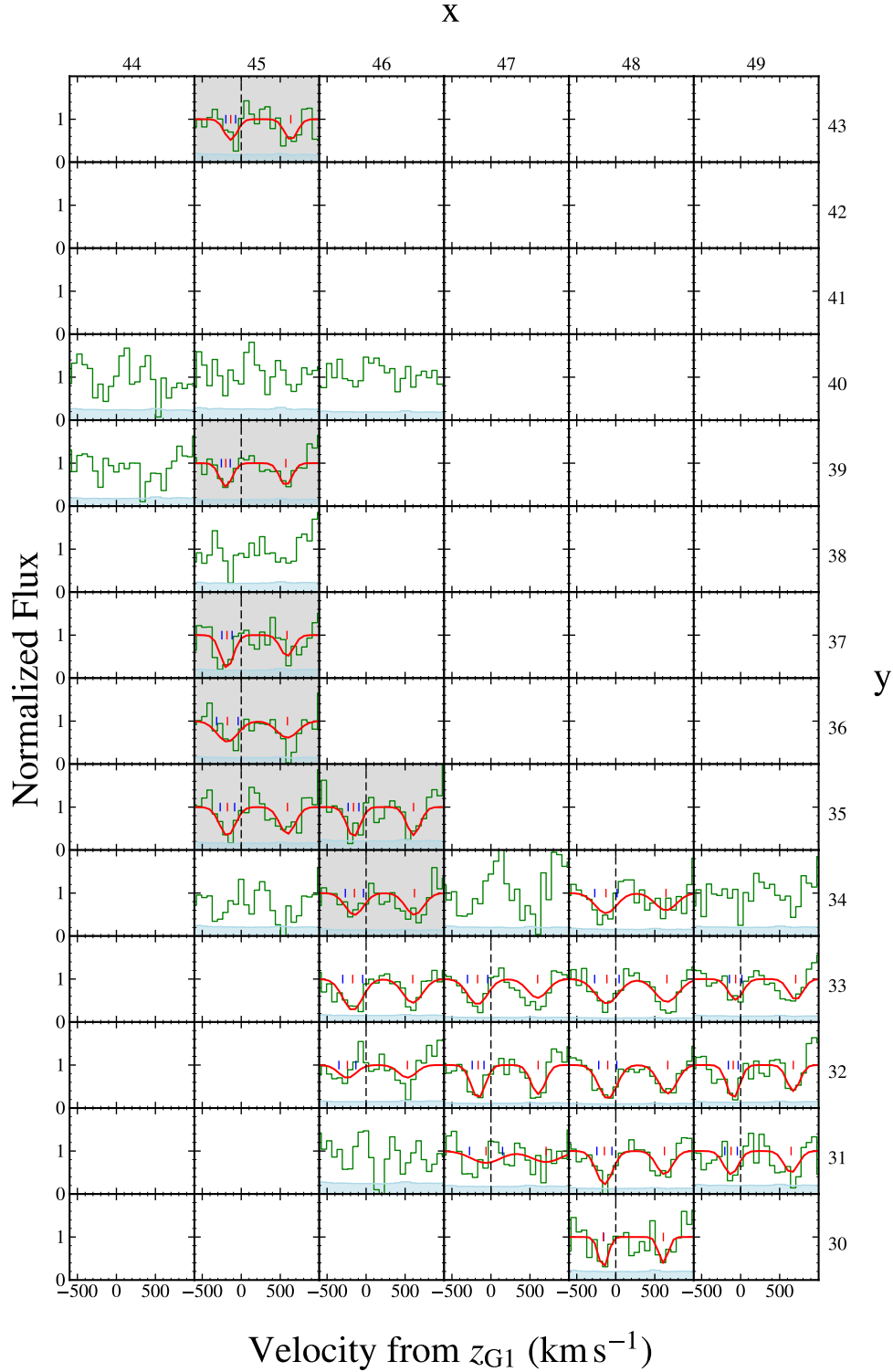


Fig. F.1: Spatial distribution of the Mg II spectra extracted over the arc images B1-B2 meeting the continuum S/N criteria in the image plane. Each panel shows the spectrum in a 4×4 ($0.8'' \times 0.8''$) binned spaxel. Green lines show the observed normalized flux, and the light blue line shows the corresponding 1σ error. Red curves show the fitted Mg II doublet when detected, and the black dashed vertical lines indicate the zero velocity of the Mg II $\lambda 2796\text{\AA}$ transition at z_{G1} . Spaxels with detected absorption are the same as in Fig. 4. Grey-coloured panels indicate transverse sightlines with detected Mg II absorption.

Appendix G: Spatial distribution of Fe II spectra

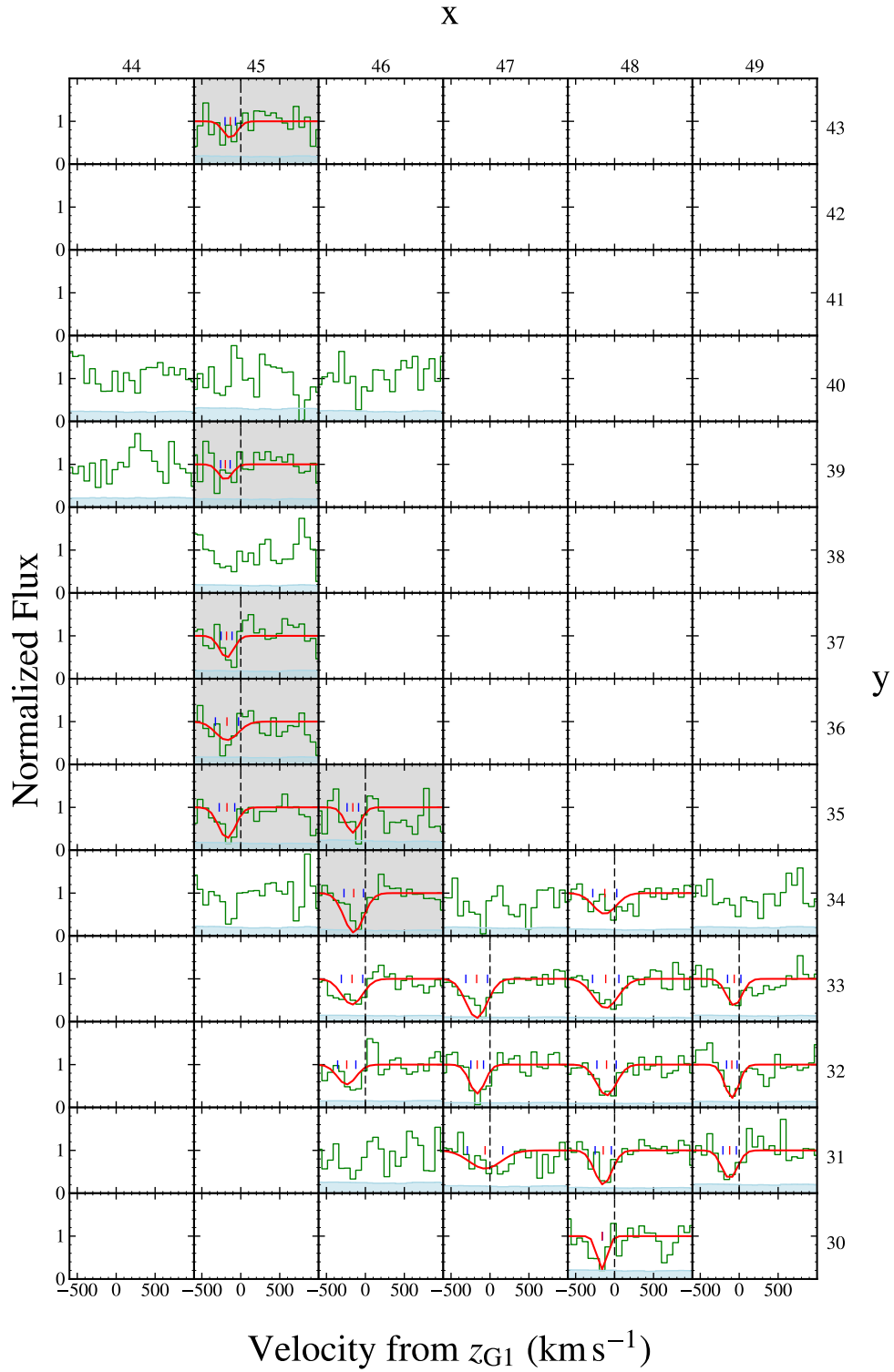


Fig. G.1: Same as Fig. F.1, but for the Fe II spectra. Black dashed vertical lines indicate the zero velocity of the Fe II $\lambda 2600\text{\AA}$ transition at z_{G1} . Grey-coloured panels indicate transverse sightlines with detected Mg II absorption.